View metadata, citation and similar papers at core.ac.uk
brought to you by CORE
provided by UNT Digital Library

National Renewable Energy Laboratory
Office of Energy Efficiency & Renewable Energy
Innovation for Our Energy Future

Development of a Wide Bandgap Cell for Thin Film Tandem Solar Cells

Final Technical Report
6 November 2003 – 5 January 2007

W. Shafarman and B. McCandless
Institute of Energy Conversion, University of Delaware
Newark, Delaware

Subcontract Report
NREL/SR-520-42388
August 2008

NREL is operated by Midwest Research Institute • Battelle   Contract No. DE-AC36-99-GO10337

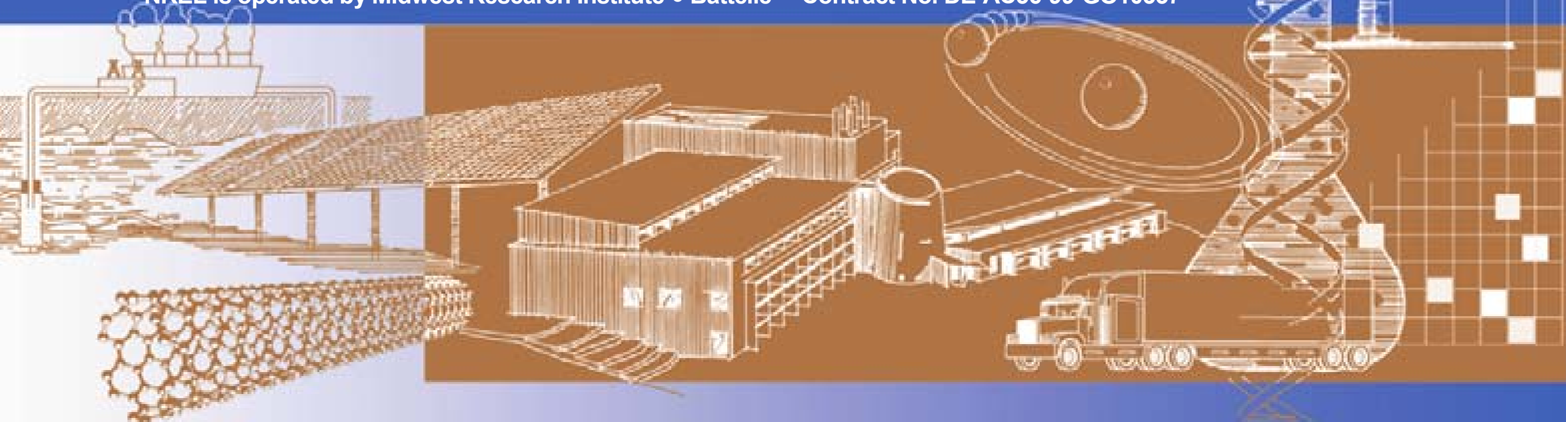

Development of a Wide Bandgap Cell for Thin Film Tandem Solar Cells

Final Technical Report
6 November 2003 – 5 January 2007

Subcontract Report
NREL/SR-520-42388
August 2008

W. Shafarman and B. McCandless
Institute of Energy Conversion, University of Delaware
Newark, Delaware

NREL Technical Monitor: Fannie Posey Eddy
Prepared under Subcontract No. XAT-4-33624-01

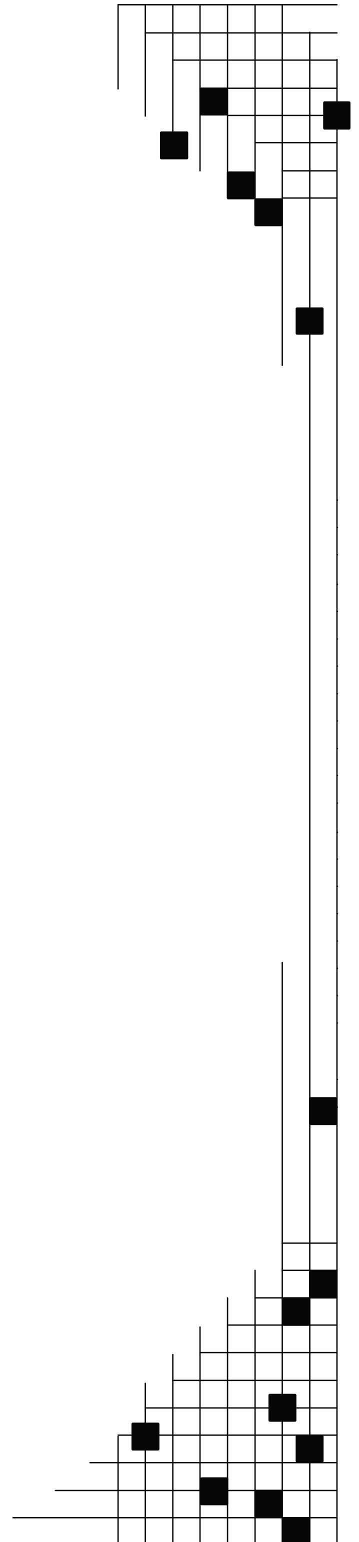

National Renewable Energy Laboratory
1617 Cole Boulevard, Golden, Colorado 80401-3393
303-275-3000 • www.nrel.gov

Operated for the U.S. Department of Energy
Office of Energy Efficiency and Renewable Energy
by Midwest Research Institute • Battelle

Contract No. DE-AC36-99-GO10337

This publication was reproduced from the best available copy submitted by the subcontractor and received no editorial review at NREL

NOTICE

This report was prepared as an account of work sponsored by an agency of the United States government. Neither the United States government nor any agency thereof, nor any of their employees, makes any warranty, express or implied, or assumes any legal liability or responsibility for the accuracy, completeness, or usefulness of any information, apparatus, product, or process disclosed, or represents that its use would not infringe privately owned rights. Reference herein to any specific commercial product, process, or service by trade name, trademark, manufacturer, or otherwise does not necessarily constitute or imply its endorsement, recommendation, or favoring by the United States government or any agency thereof. The views and opinions of authors expressed herein do not necessarily state or reflect those of the United States government or any agency thereof.

Available electronically at http://www.osti.gov/bridge

Available for a processing fee to U.S. Department of Energy
and its contractors, in paper, from:
U.S. Department of Energy
Office of Scientific and Technical Information
P.O. Box 62
Oak Ridge, TN 37831-0062
phone: 865.576.8401
fax: 865.576.5728
email: mailto:reports@adonis.osti.gov

Available for sale to the public, in paper, from:
U.S. Department of Commerce
National Technical Information Service
5285 Port Royal Road
Springfield, VA 22161
phone: 800.553.6847
fax: 703.605.6900
email: orders@ntis.fedworld.gov
online ordering: http://www.ntis.gov/ordering.htm

Printed on paper containing at least 50% wastepaper, including 20% postconsumer waste

LIST OF CONTRIBUTORS

PRINCIPAL INVESTIGATORS
William Shafarman
Brian McCandless

RESEARCHERS
Wayne Buchanan
Robert Birkmire
Steven Hegedus

POST-DOCTORAL RESEARCH FELLOWS
Greg Hanket
Shiro Nishiwaki
Alex Stavrides

TECHNICAL SUPPORT
Joshua Cadoret
Vicky DiNetta
Ronald Dozier
Kevin Hart

GRADUATE STUDENTS
Darshini Desai
Sarah Rickman
Scott Stephens
Clifford Yapp

DOCUMENT PREPARATION
Elaine Koronik

Table of Contents

1.0 Summary 1

2.0 I-III-VI2-based Solar Cells 4
- 2.1 $Cu(InGa)(SeS)_2$ Deposition 3
  - 2.1.1 Experimental Procedures for $Cu(InGa)(SeS)_2$ Deposition 4
  - 2.1.2 Results: Uniform Deposition 5
  - 2.1.3 Results: Cu-Poor Followed by Cu-Excess Growth 7
  - 2.1.4 Results: Cu-Excess Followed by Cu-Free Growth 10
  - 2.1.5 Discussion And Conclusion 16
- 2.2 $Cu(InGa)(SeS)_2$ Devices 17

3.0 CdZnTe Solar Cells 19
- 3.1 $Cd_{1-x}Zn_xTe$ Absorber Layer Thin Film Deposition 19
- 3.2 $Cd_{1-x}Zn_xTe$ Film Properties20 20
- 3.3 Post Deposition Treatment 23
- 3.4 Device Fabrication and Analysis 26

4.0 Collaborations 31
- 4.1 University of Oregon 31

List of Figures

Figure 1 Relation between the [S]/[S+Se] ratios of flux rate (Y_{flux}) and film composition (Y_{film}) 6

Figure 2 GIXRD profiles with an incidence angle of 0.5 ° and 1.0 ° for samples B2-1, B2-2. B2-3 10

Figure 3 θ-2θ XRD profiles of samples prepared by the sequential process and the reference by the uniform process 11

Figure 4 AES depth profiles (top) sample C1 and (bottom) sample C2. Measurements were done by Craig Perkins at NREL 12

Figure 5 Incidence angle dependence of GIXRD profile of (a) Cu-rich sample C3 and (b) Cu-poor sample C413

Figure 6 Change in optical bandgap by surface layer formation 14

Figure 7 GIXRD profiles from runs D (solid line), and references (dashed lines) at incidence angle of 1.0°. The dotted lines are deconvoluted profiles 15

Figure 8 Incidence angle dependence o GIXRD profile of the sample from run D: (a) GIXRD profiles, (b) area of peaks A, B, and C in Figure 8(a) 16

Figure 9 A microstructure model deduced from Figure 8 16

Figure 10 Vapor transport source ampoule geometry and obtained CdTe film thickness 20

Figure 11 Thickness (top) and EDS composition (bottom) for three 10 x 10 cm plates coated by VT with $Cd_{1-x}Zn_xTe$ using a single ampoule 22

Figure 12 Symmetric XRD patterns of the (422) and (511),(333) reflections for the three runs shown in Figure 12 22

Figure 13 XRD peak profiles of CdTe (111) before and after short $CdCl_2$ vapor treatment 24

Figure 14 XRD peak profiles of $Cd_{0.7}Zn_{0.3}Te$ (111) before and after short $CdCl_2$ vapor treatment 25
Figure 15 XRD peak profiles of $Cd_{0.2}Zn_{0.8}Te$ (111) before and after short $CdCl_2$ vapor treatment 25
Figure 16 XRD peak profiles of as-deposited ZnTe/CdS, ZnTe/ZnS and ZnTe/ZnSe on a linear intensity scale 28
Figure 17 XRD peak profiles of as-deposited ZnTe/CdS, ZnTe/ZnS and ZnTe/ZnSe on a logarithmic intensity scale to highlight weak reflections 28
Figure 18 Dark and AM1.5 JV characteristics of ZnTe/ZnS (left) and ZnTe/ZnSe (right)...... 29
Figure 19 Normalized spectral response (dark, 0V)of ZnTe/ZnS (left) and ZnTe/ZnS (right) 30
Figure 20 J-V curves of $Cu(InGa)Se_2$ devices with and without a Na diffusion barrier........... 32

List of Tables

Table I Coefficient C in Eq. 1 Used to Fit Different Compositions........7
Table II Deposition Conditions for Each Run with Time and Flux Ratios for the 1st and 2nd Layers........8
Table III Composition and Composition Ratio Analyzed by EDS Measurements of the Films' Top Side, Except Where Noted........9
Table IV J-V Parameters of $Cu(InGa)(SeS)_2$ Cells Using Process Sequences Defined in Ref. 7........18
Table V Source and Film Data for Consecutive CdZnTe Alloy Depositions Using a Single Source Ampoule and Charge........21
Table VI EDS Composition of $Cd_{1-x}Zn_xTe$ surface After Different Treatments Used for Device Fabrication........23
Table VII JV and QE Results for $Cd_{1-x}Zn_XTe$/CdS Cells treated I $CdCl_2$ vapor Figure 18. XRD peak profiles of as-deposited ZnTe/CdS, ZnTe/ZnS and ZnTe/ZnSe on a logarithmic intensity scale to highlight weak reflections........27
Table VIII JV Results for ZnTe Cells With Different Buffer Layers on ITO/BSG Substrates. Using Cu/C Back Contacts........29
Table IX $CuGaSe_2$ Devices Fabricated for Analysis at U. of Oregon........31
Table X J-V Parameters of $Cu(InGa)Se_2$ Devices With and Without a Na Diffusion Barrier, Fabricated for Analysis at U. of Oregon........31

1.0 Summary

The objective of this research program has been to develop approaches for a transparent wide bandgap cell to be used in a thin film tandem polycrystalline solar cell, which can ultimately attain 25% efficiency. Specific goals included the research and development of $Cu(InGa)(SeS)_2$ and $Cd_{1-x}Zn_xTe$ alloys with bandgap from 1.5 to 1.8 eV, demonstrating the potential of 15% cell efficiency with a transparent contact, and support of the High Performance PV Program. This Final Report presents results with an emphasis on the 3rd phase of the program.

The bandgap (E_g) of $Cu(InGa)(SeS)_2$ can be continuously varied from 1.0 to 2.7 eV by changing the relative Ga/In and S/Se compositions. The pentenary material allows E_g to be continuously varied by changing either the relative Ga/In or S/Se compositions. Work on $Cu(InGa)(SeS)_2$ has been divided into 2 areas: (1) deposition of the films with $E_g \geq$ 1.5 eV by elemental evaporation to develop methods for controlling the film composition over the entire composition range of interest, and (2) fabrication of devices and characterization to determine loss mechanisms with different deposition processes and composition. A critical issue in the evaporation and composition control for $Cu(InGa)(SeS)_2$ films has been the control of the relative S and Se compositions [1]. In this work, $Cu(InGa)(SeS)_2$ films have been prepared by thermal co-evaporation under different uniform and sequential processes to elucidate the film formation and composition control under different deposition conditions. The primary focus is on the effect of Cu-stoichiometry and process sequence on the preferred incorporation of the chalcogen species.

In films deposited with the simple process using uniform fluxes throughout the deposition, the relationship between the relative Se and S incorporation and the evaporation fluxes is established. It is shown that [S]/[Se+S] concentration in the film is dependent on whether or not the film is grown with excess Cu and further, in the case of growth with excess Cu, the relative group III composition also affects chalcogen composition. This behavior is further investigated using the deposition of $Cu_x(SeS)_y$ and $Cu(InGa)(SeS)_2$ with different sequential processes and compositions.

The option of using sequential processes, as are commonly used in the processing of high efficiency $Cu(InGa)Se_2$ solar cells, must be undertaken with caution. With sequential bi-layer processes, variations in Cu stoichiometry lead to composition gradients and inhomogeneous film formation. Depositions with different sequential processes have been used to elucidate the growth process and chalcogen incorporation.

With the sequential process of Cu-poor flux followed by Cu-excess flux, it is shown that the preferential incorporation of S occurs when both the flux and the film composition have excess Cu. There is no evidence of laterally non- uniform incorporation of S and Se in this case. With the sequential process of Cu-excess flux followed by Cu-free flux, the film initially grows with excess S. When the flux is Cu-free, the film grows inhomogeneously with two distinct regions. This includes S-rich regions which grow from the $Cu_x(SeS)_y$ phase formed under the Cu-rich flux. At the same time, growth of a

Se-rich phase is initiated, even while the film retains Cu-excess composition. This Se-rich phase continues to grow when both the film and the flux are Cu-poor. Finally, a microstructural model is proposed to explain the formation of three separate regions in the $Cu(InGa)(SeS)_2$ films grown with sequential processes.

Device related results for $Cu(InGa)(SeS)_2$ in the final phase also focused on the effects of different sequential deposition processes. Devices were fabricated with a structure of soda-lime glass / Mo / $Cu(InGa)(SeS)_2$ / CdS / ZnO / ITO / (Ni-Al grid). With the simple uniform deposition process, a reproducible baseline of efficiency > 9 % with V_{OC} > 0.8 V and FF ≈ 70 %, was established. With sequential processes including two and three-layer depositions, wide bandgap solar cells were fabricated with a much higher FF of 77-79 % than previous $Cu(InGa)(SeS)_2$ devices with different alloys.

Research under the $Cd_{1-x}Zn_xTe$ task focused on improving cell performance by controlling chemistry and materials processing during film deposition, post-deposition treatments and contact formation. During the final phase, the research approach continued to focus on chemical control of alloy composition during deposition and post-deposition treatment as well as evaluation of alternative window materials and fabrication and analysis of devices with refined processing techniques. In the previous phase of research, deposition and post deposition refinements led to $CdS/Cd_{1-x}Zn_xTe$ cells on soda-lime glass substrates with conversion efficiency >12% for E_g = 1.58 eV and efficiency > 9% for E_g = 1.6 eV [2]. No V_{OC} increase was found as bandgap was increased from 1.5 eV, but V_{OC} > 820 mV was maintained for devices with bandgap from 1.50 to 1.58 eV. At higher absorber layer band gap, for $Cd_{1-x}Zn_xTe$ films with $x > 0.20$, the obtained V_{OC} for devices with CdS window layers is < 500 mV and analysis of the junction region revealed significant intermixing, resulting in a multi-phase mixture at the interface.

The physical mechanisms of $Cd_{1-x}Zn_xTe$ alloy vapor transport deposition were further investigated to allow specification of source parameters needed to deposit films with $x \sim 0.3$. Particular emphasis was placed on determining the role of gas phase diffusion in the mixing process during vapor transport growth. Incorporation of Zn into the CdTe lattice during vapor transport growth is accomplished by entrainment of Cd, Zn and Te_2 vapors from an array of CdTe and ZnTe ingots in the single vapor transport source. Due to the isothermal nature of the source and higher CdTe partial pressure, the proportion of CdTe to ZnTe source ingot area was reduced to allow higher Zn concentration, at the expense of total growth rate.

Post-deposition processing of $CdS/Cd_{1-x}Zn_xTe$ is required to electrically activate the primary junction in the device. For cells using $Cd_{1-x}Zn_xTe$ with $x < 0.2$, two methods have been developed to yield comparable device efficiency with good retention of as-deposited Zn content and thus, absorber band gap: 1) treatment at >400°C in $ZnCl_2$ vapor or 2) very short (~1 minute) treatment at ~480°C in $CdCl_2$ vapor. In either case, some Zn is lost from the alloy absorber film. At the back surface, reaction with residual oxygen forms ZnO. In the case of $CdCl_2$, thermodynamically favored reaction between the chloride vapor and the solid alloy results in an exchange in which Zn is lost by formation

of volatile $ZnCl_2$. This process can be confined to the back surface by treatment at low $CdCl_2$ partial pressures (<10 mTorr) and short times (~1 minute). At the CdS interface, thermodynamically favorable reactivity drives the formation of ZnS and CdTe and produces a multi-phase mixture, regardless of type of chloride vapor used.

Alternative heterojunction partner materials for ZnTe with lower interface reactivity were sought and incorporated into cell structures with pure ZnTe films. A close space sublimation reactor was configured for deposition of ZnTe, ZnS and ZnSe films at temperatures from 400°C to 650°C. In addition, junctions between ZnTe and ZnO and ITO window layers were also fabricated, using sputtered window layers. Analysis of the physical properties of the cell structures showed significant interdiffusion during ZnTe deposition with CdS window layers but no detectable interdiffusion for ITO, ZnO, ZnS, or ZnSe. Devices were fabricated with $ZnCl_2$ vapor treatment and carbon contacts with and without copper. The highest V_{OC} and J_{SC} were obtained for ZnSe/ZnTe devices without copper in the contact, yielding V_{OC} ~ 600 mV and J_{SC} ~ 6 mA/cm^2.

Support of the High Performance PV Program through collaboration with other groups in the program remained an active task throughout IEC's program.

An extensive collaboration with the University of Oregon has included the preparation and characterization of controlled sets of devices with different alloy compositions, substrates, and other process variations for detailed characterization of the electronic properties of $CuInSe_2$-alloy solar cells.

Collaboration with Oregon State University focused on evaluating novel materials for such as BaCuTeF transparent back contacts to $Cu(InGa)(SeS)_2$. IEC provided substrate materials and completed fabrication and characterization of devices with these novel contacts.

The University of Toledo has been researching alternative II-VI alloys for narrow and wide bandgap cells. IEC has collaborated in the development of back contacts and processing chemistry for $Cd_{1-x}Mn_xTe$ and other II-VI alloy devices.

Finally, IEC has had many technical discussions with the above groups, the High Performance group at the National Renewable Energy Laboratory, and other University groups in the support of the overall goals of the High Performance Program.

Acknowledgments

Support from the NREL Characterization Group is gratefully acknowledged. In particular, Auger electron spectroscopy measurements were provided by Craig Perkins and EPMA measurements were provided by Bobby To.

2.0 I-III-VI2-Based Solar Cells

2.1 $Cu(InGa)(SeS)_2$ Deposition

For the deposition of $Cu(InGa)(SeS)_2$ [CIGSS], thermal co-deposition from elemental sources provides the greatest control of film composition. However, it has been reported that the Cu stoichiometry controls the preference for uptake between the volatile chalcogen species S and Se in the CIGSS during film growth [1,3]. Under Cu-excess ([Cu]>[In+Ga]) conditions, S is preferentially incorporated into the film relative to Se with [S]/[S+Se] in the film greater than in the vapor. Under Cu-poor ([Cu]<[In+Ga]) conditions, Se is preferentially incorporated into the film. This was attributed to the $Cu_x(SeS)_y$ phase which covers the CIGSS film surface during the growth [4].

For the deposition of high performance $Cu(InGa)Se_2$ absorber films, sequential depositions of Cu-poor (or Cu-free) layers and Cu-excess (or In and Ga-free) layers are commonly used [5]. Differences in grain size and a benefit in device performance with sequential processes, particularly with reduced substrate temperature, have been reported [6]. In a previous paper [7], sequential processes were used to prepare $Cu(InGa)(SeS)_2$ films. Due to the above-mentioned change in the preferential incorporation between S and Se, the sequential depositions resulted in layered $Cu(InGa)(SeS)_2$ film compositions reflecting the history of Cu stoichiometry during the growth. Furthermore, solar cells were demonstrated using the layered $Cu(InGa)(SeS)_2$ absorbers with an effective bandgap $E_g > 1.5$ (determined from quantum efficiency measurements since E_g varies through the film) with a notable fill factor of over 78 % and an efficiency of 11.9 %. However, a fundamental understanding of the formation reaction of $Cu(InGa)(SeS)_2$ under off-stoichiometric conditions is still lacking.

In this work, $Cu(InGa)(SeS)_2$ films are prepared by thermal co-evaporation under different uniform and sequential processes to elucidate the film formation and composition control under off-stoichiometric conditions. The primary focus is on the effect of Cu-stoichiometry and process sequence on the preferred incorporation of the chalcogen species. In films deposited with the simple process using uniform fluxes throughout the deposition, the relationship between the relative Se and S incorporation and the evaporation fluxes is established, and it is shown that in the case of growth with excess Cu, the relative group III composition also affects chalcogen composition. This behavior is further investigated using the deposition of $Cu_x(SeS)_y$ and $Cu(InGa)(SeS)_2$ with different sequential processes and compositions. Finally, a microstructural model for the phase structure of films grown with sequential deposition will be proposed.

2.1.1 Experimental Procedures for $Cu(InGa)(SeS)_2$ Deposition

$Cu(InGa)(SeS)_2$ films were prepared on Mo-coated and bare soda-lime glass substrates by the thermal co-evaporation of the five elements [8]. The substrate temperature, i.e. reaction temperature, was 550°C and the base pressure was 2×10^{-4} Pa. Effusion rates were determined from the measured mass loss of the element and the effective effusion duration.

For analyses, as grown and KCN etched (0.5 M, at 55 °C for 1 min) samples were used. The KCN aqueous solution selectively etches the segregated Cu-(SeS) phases caused by Cu-excess film composition. The composition was determined by energy dispersive x-ray spectroscopy (EDS) with a 20kV accelerating voltage using an Oxford Instruments, Model 6900. In a couple of cases, the compositions were also measured from the back surface side by peeling the films from the Mo back contact. As shown in previous work [9], the back surface of deposited films was smooth with no voids observed within the SEM resolution.

Compositional depth profiles were characterized by grazing incidence x-ray diffraction (GIXRD) with different incident angles using a Rigaku, D/Max-2200, and by Auger electron spectroscopy (AES) with Ar sputtering. Optical transmission and reflection were measured with a UV/VIS/NIR spectrophotometer (Perkin-Elmer, Lambda 9) equipped with an integrating sphere, using samples prepared on bare glass substrates. Relative film compositions are specified by Y and X in $Cu(In_{1-X}Ga_X)(Se_{1-Y}S_Y)_2$, i.e. X ≡ [Ga]/[In+Ga] and Y ≡ [S]/[S+Se]. Relative Cu stoichiometry is specified by the ratio Z ≡ [Cu]/[In+Ga].

Several different deposition sequences were used to characterize the growth and reaction. First, Cu-poor (Z <1) and Cu-excess (Z >1) CIGSS films and also $Cu_x(SeS)_y$ films were grown using various values for Y by a uniform deposition process with no intentional variation of fluxes throughout the deposition. Specifically, Cu-poor samples with composition ratios of Z = 0.8 - 0.9 and Cu-excess samples with Z > 1.2 were used for analyses. The Ga concentrations were controlled to give X = 0, 0.3±0.05, 0.5±0.05, or 1. All films were grown with excess chalcogen species in the flux with [S+Se]/[Cu+In+Ga]≈10, and both flux rate ratios of [S]/[Cu+In+Ga] and [Se]/[Cu+In+Ga] were greater than unity throughout all experiments.

Second, films were deposited with two sequential processes. One had a Cu-poor layer followed by a Cu-excess layer and the other a Cu-excess layer followed by a Cu-free (In-Ga-Se-S) layer. Layer compositions were changed by adjusting the Cu source temperature and to deposit the Cu-free layer, the Cu temperature was reduced below its melting temperature. In each deposition, the temperatures of the S and Se sources were fixed so that the effusion rates were expected to be constant throughout both layers of the run. The typical film was grown in 1 hour and had thickness 2 μm.

2.1.2. Results: Uniform Deposition

The uniform process was used to deposit Cu-poor CIGSS, Cu-excess CIGSS, and $Cu_x(SeS)_y$ films, and the relation between [S]/[S+Se] in the film composition (Y_{film}) and that in the vapor flux (Y_{flux}) are shown in Figure 1. This includes films with different relative Ga content X as indicated by different symbols including $CuIn(SeS)_2$ (X = 0), $Cu(InGa)(SeS)_2$ with X ≈ 0.3 and 0.5 and $CuGa(SeS)_2$ (X = 1). Open and closed symbols indicate Cu-poor and Cu-excess growth conditions, respectively. In all cases, composition was measured in the Cu-excess CIGSS after a KCN etch. The Cu-poor samples have Z = 0.8 – 0.9 except for two with Z = 0.1. For films in Figure 1, XRD

spectra (not shown) indicated a single phase with no significant peak broadening consistent with uniform through-film composition.

The data for the relative chalcogen incorporation can be described by an equilibrium reaction kinetic model developed to explain the relative incorporation of volatile As and P in the molecular beam epitaxy of GaAsP [10]. This model assumes that the S and Se incorporation in CIGSS is controlled by the kinetics of chemisorption of the chalcogen species and incorporation into the chalcopyrite lattice. This is justified by the following observations: (i) the evaporation pressure of S [11] and Se [12] is much greater than the vacuum during film growth so that the incorporation of S and Se into the film is controlled by its reaction with Cu, In, and Ga; (ii) since the reaction temperature is more than 300°C below the melting temperature of the four extremes of ternary chalcopyrites [13,14,15,16,17] the driving force to form the chalcopyrite phase from the vapor is sufficient with either S or Se [18,19,20]; and (iii) the growth rate is controlled by the fluxes of Cu, In, and Ga, and the relative compositions of the groups I and III species in the films match those of the fluxes.

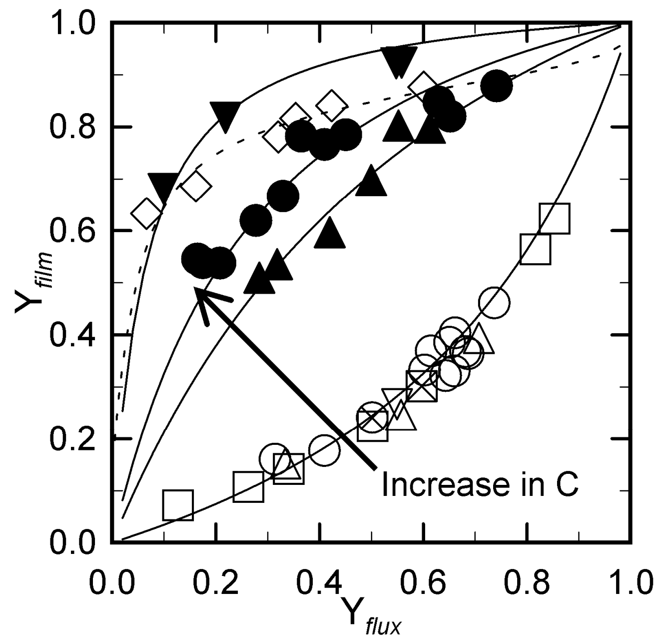

Figure 1. Relation between the [S]/[S+Se] ratios of flux rate (Y_{flux}) and film composition (Y_{film}). The shape of symbol corresponds to the relative Ga concentration X: (▲) x=0, (■) x=0.3-0.4, (●) x=0.5-0.6, and (▼) x=1, and (◇) Cu_2-α($Se_{1-y}S_y$). The open and close symbols correspond to the Cu-poor and Cu-excess deposition condition, respectively. The extreme Cu-poor compositions of $Cu_{0.1}In(SeS)_{1.6}$ (⊠) and $Cu_{0.1}Ga(SeS)_{1.7}$ (⊗) are also shown.

The solid lines in Figure 1 fitting the data for CIGSS samples were determined from the following simple equation derived from the kinetic model for chalcogen incorporation [10].

$$Y_{film}/(1-Y_{film}) = C\, Y_{flux}/(1-Y_{flux}) \quad (1)$$

where C is a function of the reaction rates of S and Se with Cu, In, and Ga and the desorption rates. These rates have Arrhenius-type temperature dependence so C is expected to be a function of temperature. If the reaction and desorption rates are independent of the relative [S] and [Se] in the flux and film and with constant reaction temperature, C reflects the relative incorporation of S against Se. An increase in C (the direction of the arrow in Figure 1) indicates an increase in the relative incorporation preference of S over Se. The functional form of Eq. 1 shows agreement with the data for CIGSS for both cases of preferred S incorporation with Cu-excess and preferred Se incorporation with Cu-poor growth. All data from Cu-poor depositions falls on one line with constant C, including the extreme Cu-poor compositions of $Cu_{0.1}In(SeS)_{1.6}$ and $Cu_{0.1}Ga(SeS)_{1.7}$, which have different crystal structures from the chalcopyrite. However, Y_{film} under Cu-excess condition depends on the relative In and Ga concentrations with each value of X described by a different value of C. The order of the preference of S versus Se is

$CuGa(SeS)_2$: Cu-excess > $CuIn(SeS)_2$: Cu-excess > $Cu(InGa)(SeS)_2$: Cu-poor

The values of C used to fit the data in Figure 1 are listed in Table I. It must be noted, however, that these values are relative to details of the deposition system since the value of Y_{flux} is determined from the source effusion rate and the actual flux at the film surface may be different due to geometric factors and secondary sources of Se and S.

In contrast to the CIGSS, $Cu_x(SeS)_y$ cannot be fit with Eq. (1). This may be due to the high re-evaporation pressure of S and Se from the solid phase [21,22,23]. The data in this case is qualitatively described by a non-equilibrium model which further accounts for the interaction between Cu-Se and Cu-S and their chemical potentials in the $Cu_x(SeS)_y$ ternary phases [24]. This is shown as a dashed line in Figure 1. Further characterization of the reaction to form $Cu_x(SeS)_y$ is not addressed in this report.

Table I. Coefficient C in Eq. 1 used to fit different compositions.

Composition	C
Cu-poor: all	0.3
Cu-excess: $CuIn(SeS)_2$	2.4
Cu-excess: $CuIn(SeS)_2$	4.3
Cu-excess: $CuIn(SeS)_2$	17

2.1.3. Results: Cu-poor followed by Cu-excess growth

For CIGSS films deposited with sequential processes, Table II provides details of the deposition sequences and Table III lists the resulting compositions measured by EDS. Runs B1 and B2 had a Cu-poor layer followed by a Cu-excess layer. For run B1, the duration of the Cu-excess 2nd layer deposition was relatively short so that the film had a final composition with Z = 0.66. For run B2, films were deposited with Z = 0.96, 1.05,

and 1.23 by taking advantage of spatial variations in the fluxes. In addition to the as-grown composition, the composition of samples B2-2 and B2-3 after a KCN etch are also shown in Table II.

Table II. Deposition conditions for each run with time and flux ratios for the 1st and 2nd layers. Values with * are target values since the effusion rate ratio could not be directly measured.

Run	Process	Deposition time (min)		Molar flux rate ratio				
				1st		2nd		Total
		1st	2nd	Z	X	Z	X	Y
B1	Cu-poor/Cu-excess	45	15	0.5*	0.6	1.6*	0.6	0.3
B2	Cu-poor/Cu-excess	30	30	0.5*	0.6	1.6*	0.6	0.3
C1	Cu-excess/Cu-free	45	15	1.2	0.6	-	0.6	0.3
C2	Cu-excess/Cu-free	30	30	1.9	0.6	-	0.6	0.3
C3	Cu-excess/Cu-free	45	15	1.5	0.6	-	0.6	0.3
C4	Cu-excess/Cu-free	45	15	1.3	0.6	-	0.6	0.3
$C_{ref}1$	Cu-excess reference	50	-	1.3	0.6	None		0.3
$C_{ref}2$	Cu-poor reference	60	-	0.8	0.6	None		0.3
D	Cu-excess/Cu-free	45	15	1.2*	0.3*	-	1	0.5
$D_{ref}1$	1st-layer reference	45	-	1.3	0.3	None		0.5
$D_{ref}2$	2nd-layer reference	45	15	1.1	1	-	1	0.5

Table III. Composition and composition ratio analyzed by EDS measurements of the films' top side, except where noted.

Sample	Comments	Composition (at%)					Composition ratio	
		[Cu]	[In]	[Ga]	[S]	[Se]	Z	Y
B1	Cu-poor	18.5	14.4	13.7	5.6	47.7	0.66	0.11
B2-1	Slightly Cu-poor	23.9	12.0	13.0	5.6	45.5	0.96	0.11
B2-2	Slightly Cu-excess	25.7	11.7	12.8	12.7	37.2	1.05	0.25
	KCN etched	25.3	11.8	12.9	12.0	38.0	1.03	0.24
B2-3	Cu-excess	28.5	10.3	12.9	25.6	22.8	1.23	0.53
	KCN etched	26.4	11.0	13.6	22.4	26.6	1.08	0.46
C1	Device process	21.9	10.7	15.4	19.6	32.4	0.84	0.38
	Back side	25.6	11.8	13.8	32.9	15.9	1.00	0.67
C2	Long Cu-free stage	21.9	10.2	16.9	13.6	37.4	0.81	0.27
	Back side	25.5	11.8	13.4	34.3	14.9	1.01	0.70
C3	Cu-excess	27.8	10.7	13.6	26.7	21.3	1.14	0.56
	KCN etched	26.3	11.0	13.8	26.3	22.5	1.06	0.54
C4	Slightly Cu-poor	24.4	10.5	14.9	20.3	29.8	0.96	0.41
$C_{ref}1$	Reference, Cu-excess	29.9	10.2	12.2	31.5	16.3	1.34	0.66
	KCN etched	25.7	11.2	14.0	30.4	18.7	1.02	0.62
$C_{ref}2$	Reference, Cu-poor	22.0	11.0	16.0	8.2	42.9	0.81	0.16
D	Ga-S-Se on Cu-excess CIGSS	20.7	10.5	15.4	32.8	20.7	0.80	0.61
$D_{ref}1$	Cu-excess	30.3	15.6	5.1	40.3	8.7	1.46	0.82
	KCN etched	25.4	17.6	6.9	40.1	10.1	1.04	0.80
$D_{ref}2$	Ga-S-Se on Cu-excess CGSS	21.2	0.0	24.7	35.2	18.9	0.86	0.65

Despite the Cu-excess flux during the second step of the depositions, Cu-poor samples B1 and B2-1 had similar Se-rich composition with the relation between Y_{film} and Y_{flux} in good agreement with the results using uniform Cu-poor deposition shown in Figure 1. In samples B2-2 and B2-3 which changed from Cu-poor to Cu-excess during growth, Y_{film} increased with increasing excess Cu content, even after the KCN etch. Figure 2 shows GIXRD profiles of the (112) and (103) peaks for samples B2-1, B2-2, and B2-3 measured using incident angles of 0.5° and 1.0° corresponding to sampling depths of ~ 200 nm and ~400 nm respectively. Samples B2-2 and B2-3 were measured after the etch and in all films only the chalcopyrite phase of $Cu(InGa)(SeS)_2$ was observed.

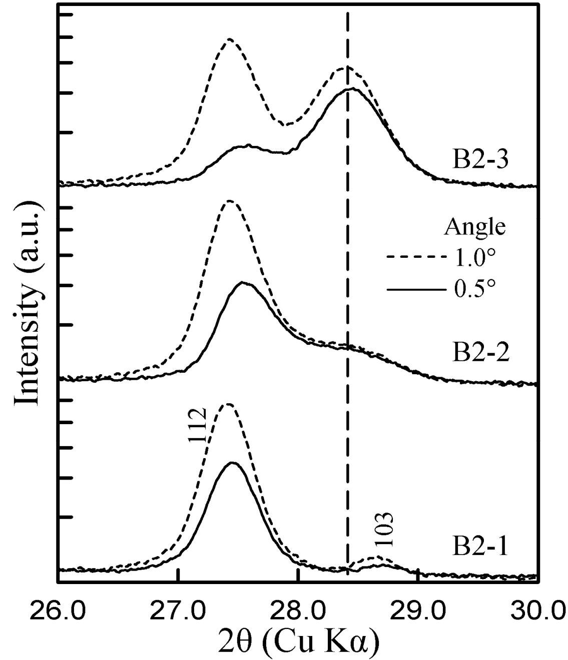

Figure 2. GIXRD profiles with an incidence angle of 0.5 ° and 1.0 for samples B2-1, B2-2. B2-3.

In sample B2-1, there is no indication of a second phase. However, samples B2-2 and B2-3 have an additional peak (indicated by the dashed line) at $2\theta \approx 28.5°$ between the (112) and (103) peaks for sample B2-1. The relative change in the intensities of the peaks at ~27.5° and ~28.5° with incident angle indicates that the peak at 28.5 ° is due to a phase with smaller lattice constant segregated at the film surface. The intensity from the surface phase follows the increase in Y_{film} from sample B2-2 to B2-3. Considering the composition and preparation sequence, it is reasonable to identify the surface phase as a chalcopyrite CIGSS with greater relative S concentration than the bottom layer. Assuming the surface phase grows after the film attains Cu-excess composition, its thickness is estimated from the deposition rate and the GIXRD data to be about 120 nm and 480 nm for samples B2-2 and B2-3, respectively.

It is clear that the surface S-rich phase is not initiated until a Cu-excess film composition is reached. The preferred incorporation of S over Se ($Y_{film} > Y_{flux}$) requires both the Cu-excess flux and the formation of $Cu_x(SeS)_y$ together with the CIGSS.

2.1.4. Results: Cu-excess followed by Cu-free growth

Samples C1 to C4 were deposited using a layer with Cu-excess flux followed by a layer with Cu-free flux, with different times and Cu effusion rates. Again, the deposition conditions are summarized in Table II and the resulting compositions in Table III. Run C1 is the baseline process used previously for device characterization [7] which gave Z = 0.84 in the completed film. In run C2, the relative deposition times of the Cu-excess and Cu-free layers was changed from 3:1 to 1:1 and the Cu effusion rate during Cu-excess

deposition was increased so that the film had comparable Cu content to that C1. In runs C3 and C4, the Cu effusion rates were greater than in C1. Run $C_{ref}1$ and $C_{ref}2$ are reference films for comparison with uniform Cu-excess and Cu-poor depositions, respectively. In Table III, compositions of samples C1 and C2 measured from the back side are also listed as are the compositions of C3 and $C_{ref}1$ after a KCN etch.

Figure 3 shows XRD (112) peak profiles of samples C1 and C2 along with reference samples $C_{ref}1$ (KCN etched) and run $C_{ref}2$. The samples from run C1 and run C2 show two distinct peaks, which is typical for a 2-layer structure [6]. The position of the peaks is similar but the relative intensities correlate to the difference in the relative deposition times of the Cu-excess and Cu-free layers. The peak positions are also similar to the references samples for Cu-excess and Cu-poor growth with comparable fluxes.

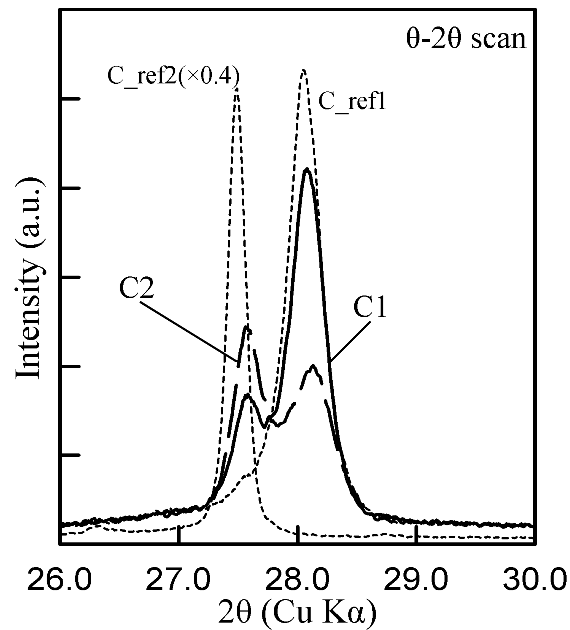

Figure 3. θ-2θ XRD profiles of samples prepared by the sequential process and the reference by the uniform process.

Compositional depth profiles, measured by AES, of samples C1 and C2 are shown in Figure 4. From the top surface to the bottom, both films have a decrease in [Se] and an increase in [S] and [Cu], while [In] and [Ga] are constant. The film grown with the shorter 15 min Cu-free layer (run C1) shows a steeper composition gradient than the film grown with the longer 30 min Cu-free layer (run C2). The sharp XRD peaks in Figure 4 suggest two regions with distinctly different compositions, in contrast to the broad change in [S] and [Se] suggested by the AES profiles. This difference may result from laterally inhomogeneous compositions and/or from smearing of the composition caused by the sputtering used for the AES profiles. The values of Z determined from the AES are believed to be higher than the EDS values because of preferential sputtering effects, particularly for S, during the depth profile measurements. The AES profile of [Cu] is probably correlated with [S]. Nevertheless, the decrease in Cu concentration in the AES

profiles from the bulk toward the surface is consistent with the composition of the surface side and the backside in Table II. From the surface side, the films from runs C1 and C2 have Z=0.84 and 0.81, respectively, whereas from the backside both films have Z=1.0.

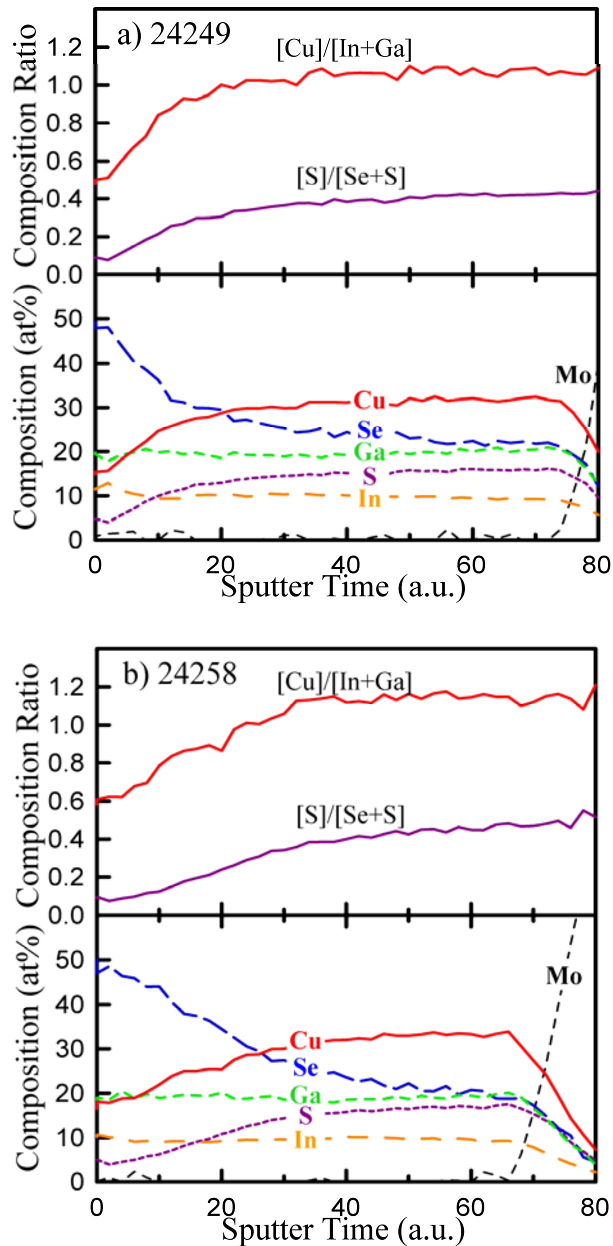

Figure 4. AES depth profiles (top) sample C1 and (bottom) sample C2. Measurements were done by Craig Perkins at NREL.

Figure 5 shows GIXRD profiles of KCN etched Cu-excess (run C3) and slightly Cu-poor (run C4) films. Both films show the same characteristic two-layer structure of a top layer with greater lattice constants which mainly dominate the spectra at low incident angle, and a bottom layer with smaller lattice constants. This shows that the [S]/[S+Se] gradient forms as a result of the change in flux. The two-layer structure also controls the optical transmission as shown in Figure 6. The normalized transmission T/(1-R), where T and R are the total transmission and reflection, is shown for films deposited on bare soda lime glass in the same two runs as the films on glass Mo substrates characterized above. C3 and C4 have similar absorption edge wavelength which is determined by the top Se-rich layer due to its narrower bandgap than the bottom S-rich layer. For comparison, the absorption edge in $C_{ref}1$ is shifted to lower wavelength since it contains no Se-rich layer. It should be mentioned that the KCN etched Cu-excess films show high optical absorption below the bandgap, but this topic is beyond the scope of this work.

The results in Figures 5 and 6 show that the growth of the Se-rich layer is initiated with Cu-excess composition during the Cu-free flux of this deposition process and does not require a change in the film composition from Cu-excess to Cu-poor. This also explains the observations in Figure 3, where a change in the relative intensity of the two peaks depends on the relative deposition times of Cu-excess and Cu-free stages.

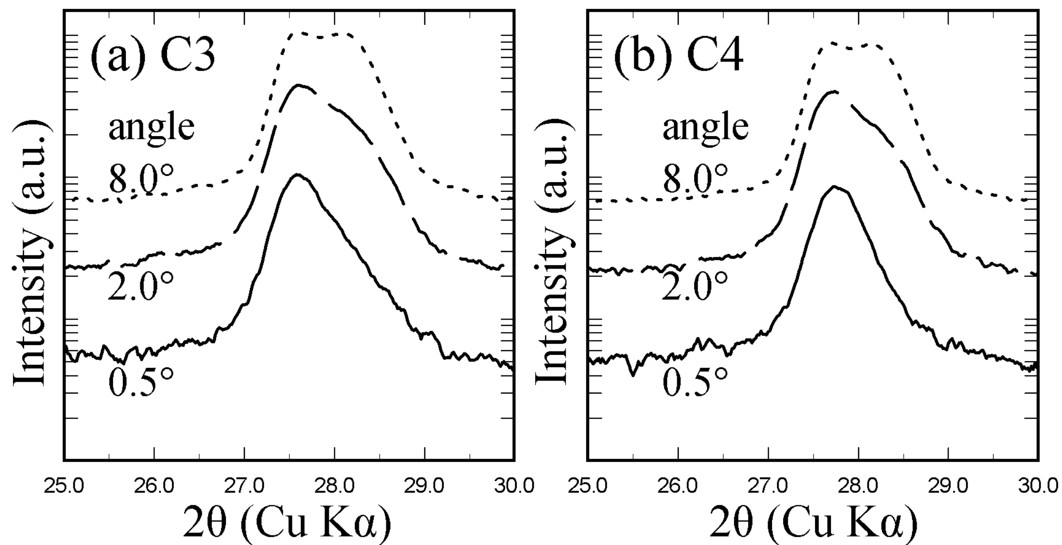

Figure 5. Incidence angle dependence of GIXRD profile of (a) Cu-rich sample C3 and (b) Cu-poor sample C4.

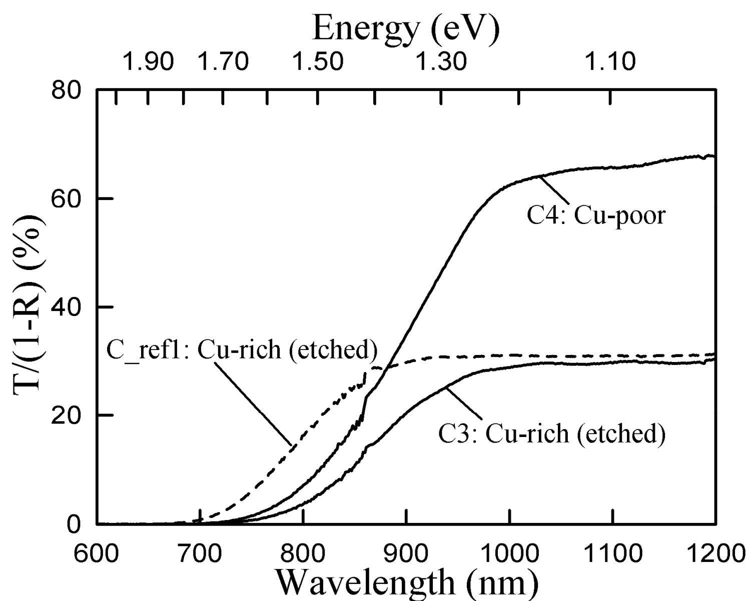

Figure 6. Change in optical bandgap by surface layer formation.

Film growth during the stage when the flux is Cu-free but the film still contains excess Cu is better understood by considering Sample D. This was also deposited with a sequential process which had CIGSS grown with Cu-excess flux followed a Cu-free flux but in this case, the Cu-free layer had only Ga, S, and Se. This is compared to a uniform layer Cu-excess deposition $D_{ref}1$ of CIGSS with the same flux conditions as the first layer of run D and to run $D_{ref}2$ which had $CuGa(SeS)_2$ (CGSS) by a sequential deposition process with the same S and Se flux rates in each layer.

XRD analysis distinguishes three different regions in Sample D. Figure 7 shows the GIXRD profiles at incident angle = 1° along with profiles from the reference samples, shown as dashed lines, and deconvoluted peak profiles, shown as dotted lines. The uniform deposition $D_{ref}1$, shown after the KCN etch, gave a single peak consistent with the measured composition. Sample $D_{ref}2$, from the sequential layer deposition has a peak doublet corresponding to higher and lower [S]/[S+Se]. For run D, three peaks are observed. Peak A at the lowest angle is attributed to a high S CIGSS layer deposited under the Cu-excess stage, corresponding to the peak from sample $D_{ref}1$. Peaks B and C are comparable to those from run $D_{ref}2$. Specifically, the lower angle peak B can be attributed to a Se-rich $CuGa(SeS)_2$ phase, and the higher angle peak C is due to S-rich $CuGa(SeS)_2$. It is concluded that the S-rich CGSS phase was formed during the Cu-free growth stage using Cu as well as S and Se from the Cu-excess layer in the film. Once this layer was consumed, the Se-rich layer was grown.

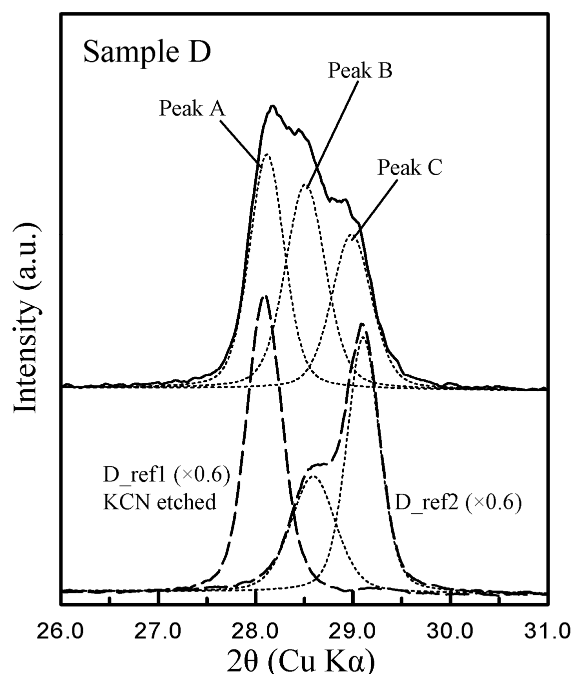

Figure 7. GIXRD profiles from runs D (solid line), and references (dashed lines) at incidence angle of 1.0°. The dotted lines are deconvoluted profiles.

A model for the film microstructure formed by this process can be proposed based on the XRD profiles. For run D, Figure 8(a) shows the incident angle dependence of the diffraction profile, and Figure 8(b) shows the areas of deconvoluted peaks calculated from the profiles. For 0.5° incident angle which is only sensitive to the near surface (~0.2 μm), the contribution to the profile is mainly from peak B with smaller peak C. With increasing incident angle corresponding to sampling deeper into the film, the intensities of peak A and peak C increase linearly, as shown in Figure 8(b) and its inset. The intensity of peak B saturates above 2.0° incident angle. Based on these results, a model of the film structure prepared by this sequential process is proposed, as shown in Figure 9. The film consists of three regions corresponding to the three XRD peak positions. Sequentially, region A is the S-rich CIGSS layer grown in the Cu-excess 1st layer. Then region C is formed with Cu-free flux using Cu, Se, and S deposited during the Cu-excess stage in addition to the arriving Ga, Se, and S species. At the same time, region B with higher Se content grows when the arriving Cu-free flux reacts only with Cu diffusing from the underlying layers and continues when there is no excess Cu phase in the film. In this experiment with no In in the Cu-free flux, the regions C and B could be distinguished as originating from the Cu-free flux with or without Cu, Se, and S from the underlying $Cu_x(SeS)_y$ phase, respectively. This microstructural picture determined by the incident angle dependence illustrates that the film grows with laterally as well as vertically segregated regions under these two different conditions. In Figure 5, regions C and B could not be distinguished.

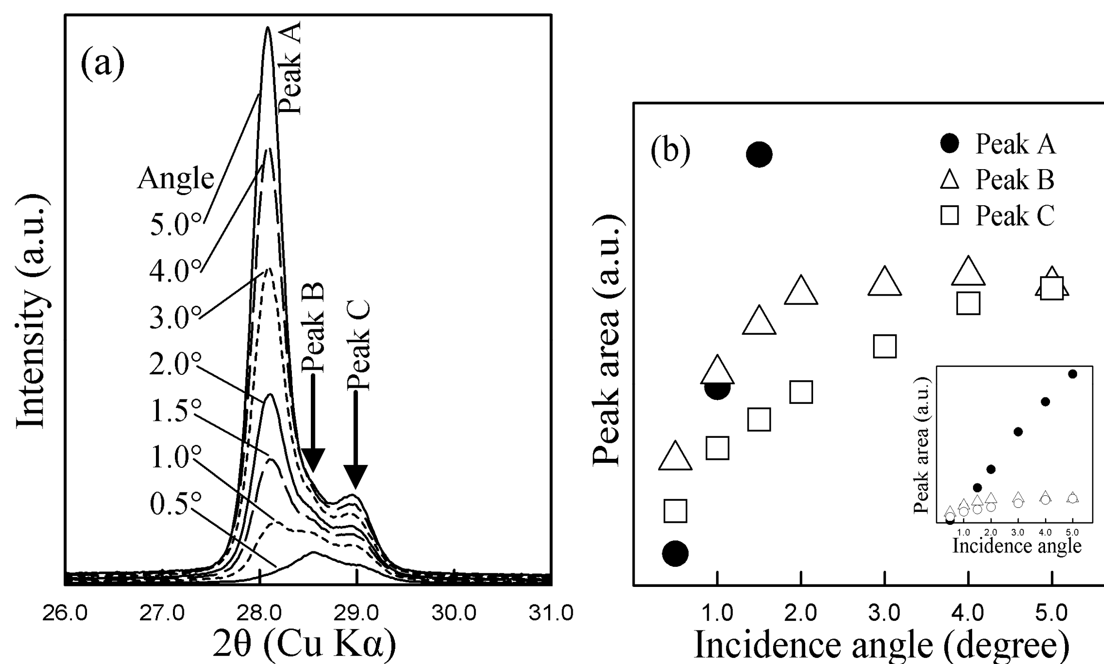

Figure 8. Incidence angle dependence of GIXRD profile of the sample from run D: (a) GIXRD profiles, (b) area of peaks A, B, and C in Figure 8(a).

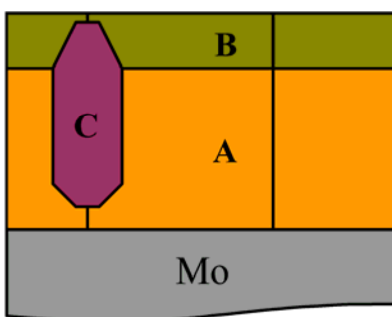

Figure 9. A microstructure model deduced from Figure 8. Region A is grown during Cu-excess 1st layer deposition. Region B is grown during Cu-free deposition. Region C is formed during Cu-free stage, and distributes between layers A and B.

2.1.5. Discussion and Conclusion

With uniform deposition of CIGSS at 550°C, the incorporation of volatile Se and S into the chalcopyrite film depends on the Cu stoichiometry and, for the case of growth with excess Cu, the relative group VI composition. It was proposed that the chalcogen composition is determined by the kinetics of surface adsorption and desorption, rates of reaction with the Cu, In, and Ga, and incorporation into the lattice. The general form of the kinetic model derived to explain the incorporation of volatile species in III-V alloys allows a good fit to all the CIGSS films in Figure 1. To quantitatively compare such a kinetic reaction model with the observed film growth and composition would require

direct measurement of the rates of reaction and desorption. Lacking such knowledge, Eq. 1 provides an empirical fit that can be used to predict the film composition from knowledge of the fluxes at the surface.

There are several aspects of the growth and reaction to form CIGSS which are not explained. In particular, the difference between Cu-excess case and Cu-poor case is not understood. A difference in the reaction pathway to form CIGSS is a possibility. However, it was shown that $Cu_x(SeS)_y$ does not fit the form of Eq. 1 so this phase apparently does not serve as a precursor or a template which determines the relative incorporation of S and Se.

In addition, the polymeric nature of the evaporated S and Se species incident on the substrate can be expected to affect the reaction kinetics. This could be characterized with sources which crack or otherwise reduce the polymer to dimer or monomer species. The effect of substrate temperature also is not established although it is anticipated that the chalcogen incorporation will depend on temperature.

With the sequential process of Cu-poor flux followed by Cu-excess flux, it was shown that the preferential incorporation of S only occurs when both the flux and the film composition have excess Cu. There is no evidence of laterally non- uniform incorporation of S and Se in this case. With the sequential process of Cu-excess flux followed by Cu-free flux, the film initially grows with excess S. When the flux is Cu-free, the film grows inhomogeneously with two distinct regions. This includes S-rich regions which grow from the $Cu_x(SeS)_y$ phase formed under the Cu-rich flux. At the same time, growth of a Se-rich phase is initiated even while the film retains Cu-excess composition. This Se-rich phase continues to grow when both the film and the flux are Cu-poor.

In conclusion, the deposition of CIGSS with predictable control of composition is complicated by the dependence of the incorporation of volatile Se and S on film stoichiometry. The composition using a uniform process can be predicted using Eq. 1 even though a complete model of the relation between flux composition and film composition is not available. The option of using sequential processes, as are commonly used in the processing of high efficiency $Cu(InGa)Se_2$ solar cells must be undertaken with caution. With sequential bi-layer processes, variations in Cu stoichiometry can lead to composition gradients and inhomogeneous film formation.

2.2 $Cu(InGa)(SeS)_2$ Devices

Device results were presented in a paper "Preparation Of Wide Bandgap $Cu(InGa)(SeS)_2$ Solar Cells With Improved Fill Factor," by Shiro Nishiwaki and William Shafarman, at the 4th World Conference on Photovoltaic Energy Conversion [7]. In this work, $Cu(InGa)(SeS)_2$ absorber films with a bandgap $E_g \geq 1.5$ eV have been prepared using thermal co-evaporation with different sequences of Cu rich and Cu poor deposition. The composition through the film is, in some cases, non-uniform due to changes in relative S and Se incorporation. The compositional depth profile was characterized by GIXRD and

Auger electron spectroscopy with Ar sputtering. The composition ratio [S]/[S+Se] in the films depends on the process and the composition ratio [Cu]/[In+Ga] during deposition. Several different processes with single-layer, two-layer, and three-layer sequences were compared.

The best device results with a soda-lime glass/Mo/Cu(InGa)$(SeS)_2$/CdS/ZnO/ITO/(Ni-Al grid) structure with each are shown in Table IV. These results are all on cells with no anti-reflection layer. Of particular note, solar cells were fabricated with a much higher FF > 77 % than previous wide bandgap Cu(InGa)$(SeS)_2$ devices. Quantum efficiency of the Cu(InGa)$(SeS)_2$ cells shows relatively poor response for wavelength > 600 nm compared to that with $CuInS_2$.

There are still several unresolved issues related to the film growth, including the mechanism controlling the relative chalcogen incorporation, and the device behavior, including understanding the limitations to the current collection length. Nevertheless, the above results encourage utilizing Cu(InGa)$(SeS)_2$ as an absorber for the wide bandgap solar cells.

Table IV. J-V parameters of Cu(InGa)$(SeS)_2$ cells using process sequences defined in Ref. 7. Eg is estimated from the EDS composition for one-layer, and from the QE curve for the others by comparing it with that of the one-layer device.

Process	E_g (eV)	Eff. (%)	V_{OC} (V)	J_{SC} (mA/cm^2)	FF (%)
One-layer	1.55	10.3	0.804	17.2	74.7
	1.6	9.4	0.863	15.6	70.1
Two-layer	1.5	11.2	0.760	19.2	77.3
	1.55	10.5	0.802	17.0	76.7
Three-layer	1.5	10.9	0.825	17.0	77.7
	1.55	9.7	0.795	15.5	78.8
3-stage	1.55	9.9	0.815	15.4	78.7
	1.6	8.8	0.881	12.7	78.6

3.0 CdZnTe Solar Cells

3.1 $Cd_{1-x}Zn_xTe$ Absorber Layer Thin Film Deposition

Despite the demonstrated reproducibility of $Cd_{1-x}Zn_xTe$ alloy thin film deposition over a modest compositional range, $0 < x < 0.25$, using vapor transport, a quantitative understanding of vapor delivery and compositional uniformity is still required for control at higher alloy compositions. The vapor transport method for obtaining uniform alloy thin films was modified for suppression of Cd and Te_2 partial pressures using a spaced array of CdTe and ZnTe ingots [2]. A quantitative assessment of the alloy vapor transport process requires separation of under-saturation conditions (mass transfer dynamics) from thermodynamic effects (mixing effects). Experiments were conducted to determine the magnitude of the diffusivity and mixing in the source manifold by depositing CdTe films from source ampoules containing less surface area than required for saturation at 850ºC and 20 sccm carrier gas flow rate, at total pressure = 20 Torr. Two configurations were employed as shown in Figure 10. The upper schematic depicts the condition used to deposit $Cd_{1-x}Zn_xTe$, with CdTe ingots evenly spaced within the ampoule. The evenly spaced CdTe ingots show monotonic cross-web development of vapor saturation, determined from thickness of the resulting CdTe film at the substrate (550ºC). The upper data points show that the CdTe thickness varied by 2x across the deposition zone. By clumping ingots together at the closed end of the source ampoule, an estimate of the diffusion and mixing contribution to the net film growth can be determined (lower schematic). Indeed, the lower set of data points shows significant diffusion contribution to mass transfer. The vapor transport model for CdTe deposition at 20 Torr, 20 sccm, 850ºC, in He, yields a residence time $\tau_R = 0.15$ sec and characteristic diffusion time $\tau_D = 0.5$ sec. These values are in qualitative agreement with the observed 3X variation in film growth across the deposition zone (lower case). If $\tau_D \sim \tau_R$, only ~30% variation in growth is expected.

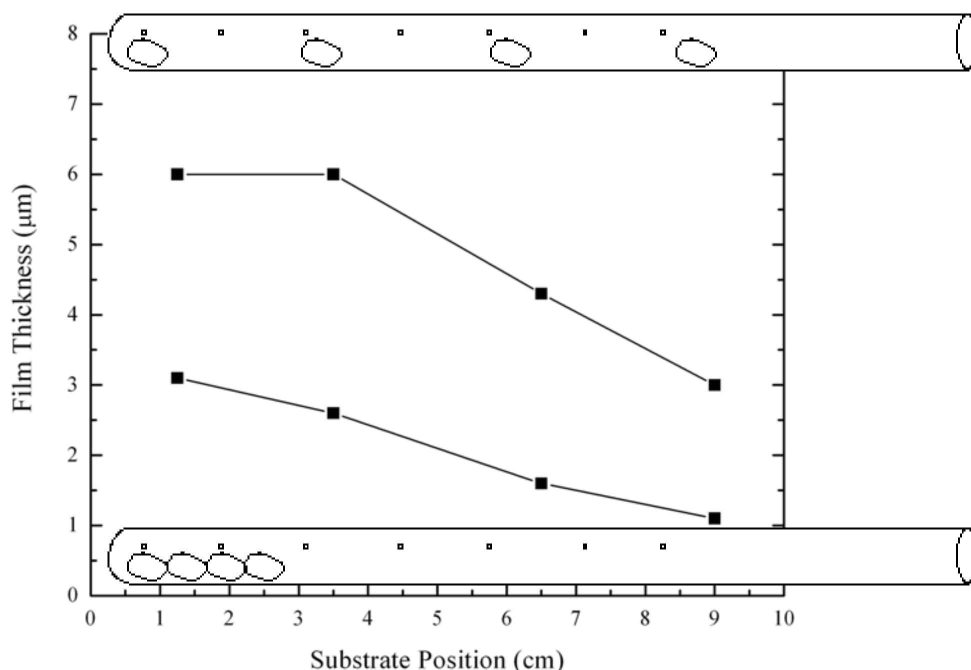

Figure 10. Vapor transport source ampoule geometry and obtained CdTe film thickness.

The results for CdTe deposition would suggest a strong variation on Cd/Zn composition and total film thickness across the deposition zone, since ample ZnTe ingot surface area is present for vapor saturation with Zn and Te_2. The measured $Cd_{1-x}Zn_xTe$ film composition and thickness show a weaker dependence with position. For a film 4 µm thick with x = 0.2 in the center of the 10 cm x 10 cm plate, the total thickness variation is 0.33 µm and compositional variation is $0.18 < x < 0.22$. This suggests that additional mixing occurs. The formation of an alloy coating on all the source ingots and Zn vapor phase mixing are possible as mechanisms to explain the observed uniformity in film thickness and composition.

3.2 $Cd_{1-x}Zn_xTe$ Film Properties

$Cd_{1-x}Zn_xTe$ films were routinely deposited by vapor transport onto 10 x 10 cm substrates using source ampoules charged with 6N purity CdTe and ZnTe crystals in the proportion 1:4. Substrates were Pilkington TEC15 coated with a Ga_2O_3 buffer layer and a window layer, typically CdS. In evaluating effusion rate and film composition from a given source ampoule, we found that the mean film thickness decreased while the composition, x, increased over time for a given source ampoule charged with CdTe and ZnTe ingots. The decrease in overall growth rate is attributed to a decrease in exposed CdTe surface area within the source over time, due to sintering and alloying of the mixed charge. The mean film composition therefore increases while the compositional uniformity, as measured by EDS of the exposed surface, decreases. Thickness and compositional results for three consecutive depositions (runs) using the same source ampoule are shown

in Figure 11. The ampoule effusion rate and mean film properties for these runs are summarized in Table V. Note that several pure CdTe runs using a separate ampoule were performed between the first (VT233) and second runs (VT245) and that the charged alloy ampoule was stored under vacuum. For the second (VT245) and third (VT246) runs with the given source ampoule, the leading edge and the far side from carrier gas inlet have considerably lower Zn content than the remainder of the substrate. XRD analysis (Fig. 12) shows that the gross run-to-run differences in average composition are real, i.e., not surface artifacts or significant through-film variations, and therefore, reflect changes within the source itself. The average compositions by the XRD method are comparable to the mean areal values determined by EDS: VT233, x = 0.10; VT245, x = 0.18; and VT246, x = 0.23. Furthermore, the large statistical variation of composition in the second and third runs is qualitatively suggested by broadening of the XRD peaks in Figure 12 and is attributed to lateral effects. Through-film uniformity was verified by GIXRD at multiple incident angles and therefore sampling depths.

Table V. Source and film data for consecutive CdZnTe alloy depositions using a single source ampoule and charge.

Run	Ampoule loss rate x 10^{-6} (mol/s)	Film growth rate x 10^{-6} (mol/s)	Mean film composition by XRD (x)	Mean film composition by EDS (x)	Areal variation in composition (± x)
233	2.33	1.36	0.10	0.12	0.02
245	2.20	1.31	0.18	0.18	0.10
246	1.53	0.94	0.23	0.26	0.13

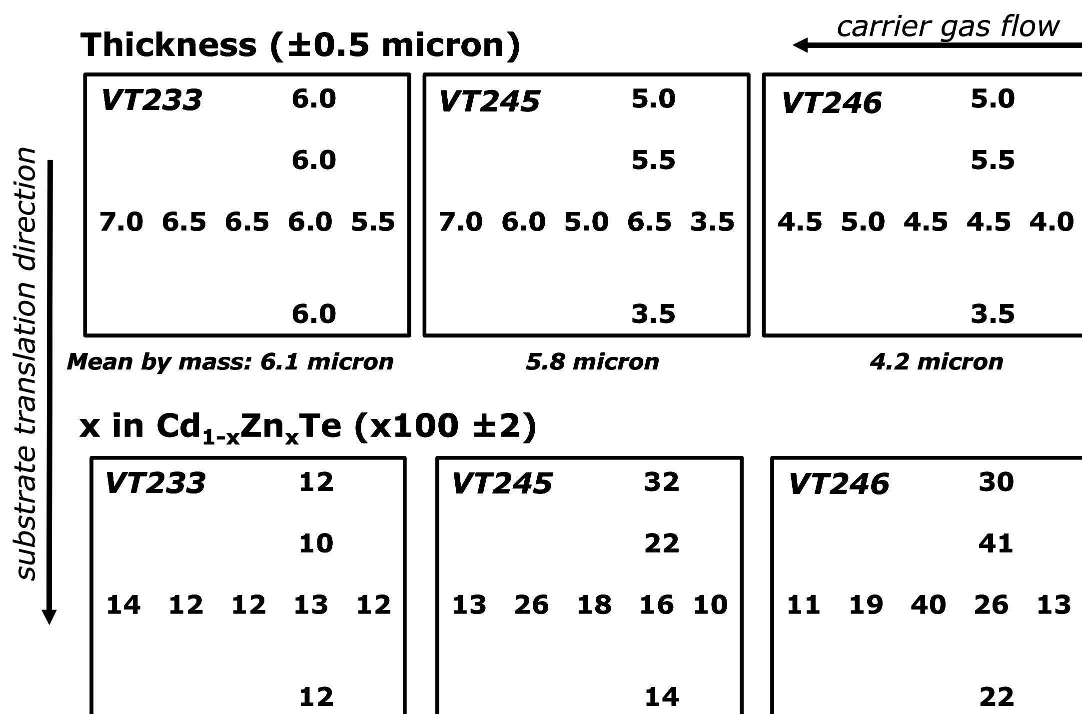

Figure 11. Thickness (top) and EDS composition (bottom) for three 10 x 10 cm plates coated by VT with $Cd_{1-x}Zn_xTe$ using a single ampoule. During deposition, the leading edge is at the bottom of each plate and the carrier gas enters the ampoule from the right.

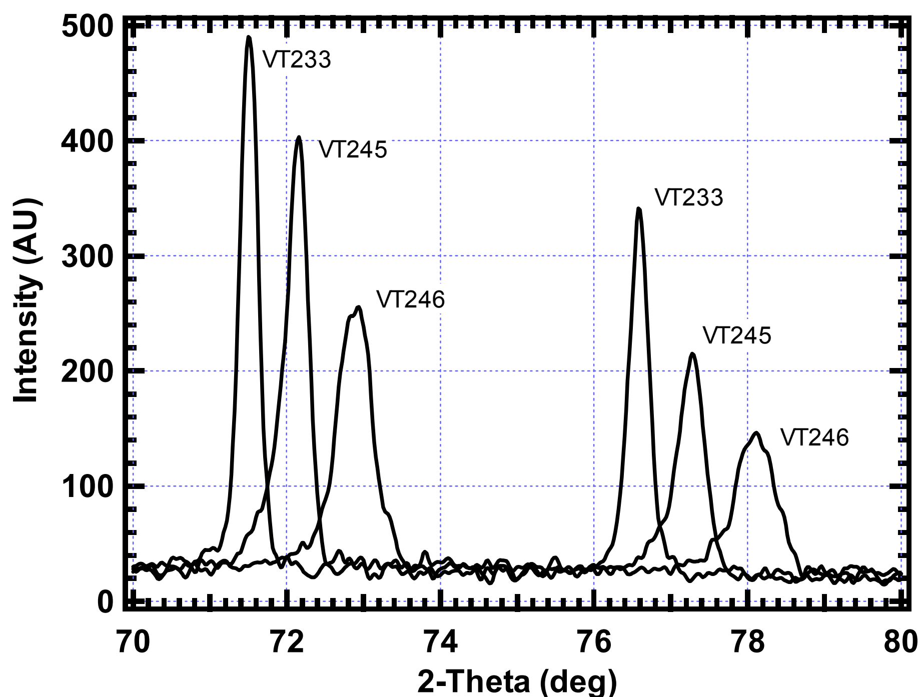

Figure 12. Symmetric XRD patterns of the (422) and (511),(333) reflections for the three runs shown in Figure 11. Data taken with Cu-kα radiation at 35 kV and 20 mA.

3.3 Post Deposition Treatment

Options for post-deposition processing of $Cd_{1-x}Zn_xTe$/CdS solar cells continue to be explored, in particular controlling the chemistry of the alloy film during the high temperature anneal and vapor halide treatments. A significant development of research during this contract is that the vapor halide treatment approach offers flexibility in the choice of halide when short treatment times are employed. This is borne out by measurements at surface composition on alloy films before and after treatments. Table VI lists energy dispersive x-ray spectroscopy (EDS) compositions for the surfaces of $Cd_{1-x}Zn_xTe$ films from a single VT deposition. The beam energy was 20 kV, which corresponds to a sampling depth (SD) of ~1.6 µm. Sample 211.3 corresponds to the baseline process developed in 2005, using a 600ºC anneal in H_2/Ar followed by a 20 minute treatment at 400ºC in ~1 mTorr $ZnCl_2$ vapor. The EDS composition of the back surface of the $Cd_{0.8}Zn_{0.2}Te$ remained unchanged throughout the processing.

Table VI. EDS composition of Cd1-xZnxTe surface after different treatments used for device fabrication.

Piece VT	Condition	EDS 20kV, SD ~ 1.6 m (x ±0.01)
211.1	As Deposited	0.22
211.1	+HT 650ºC, 20 min, H_2/Ar	0.23
211.1	+Vapor $CdCl_2$ 480ºC, 2 min, Ar	0.12
211.2	As Deposited	0.20
211.2	+HT 600ºC, 20 min, H_2/Ar	0.20
211.2	+Vapor $CdCl_2$ 480ºC, 2 min, Ar	0.10*
211.3	As Deposited	0.21
211.3	+HT 600ºC, 20 min, H_2/Ar	0.21
211.3	+Vapor $ZnCl_2$ 400ºC, 20 min, Ar	0.21

*Note: x = 0.12 at 30kV, SD ~ 3.5 µm

Sample VT211.2 utilized the same high temperature anneal but was then treated in $CdCl_2$ vapor for 2 minutes at 480ºC. In this case, the anneal step produced no detectable change in surface composition and the $CdCl_2$ treatment reduced the Zn content by ~2x in the near-surface region. A measurement at higher beam energy, 30 kV, shows an increase in Zn content, supporting the view that the Zn is preferentially removed from the film via a diffusion-limited process and strong chemical reaction when using $CdCl_2$ vapor. Experience with $CdCl_2$ treatments of CdTe/CdS shows a strong dependence of grain boundary Cd and S diffusion in CdTe on the $CdCl_2$ and O_2 concentration in the vapor. For the present study, the O_2 pressure is residual (<0.1 mTorr) and the $CdCl_2$ pressure was ~1 mTorr. At these concentrations the diffusion process is relatively slow compared to the time needed to electrically activate the films allowing short $CdCl_2$ treatments to be employed for $Cd_{1-x}Zn_xTe$ solar cell processing.

Sample VT211.1 utilized the same $CdCl_2$ treatment as VT211.2 but was annealed at 650ºC prior to the halide treatment. The compositional results are qualitatively similar to those for VT211.2, with reduction of Zn content at the back of the $Cd_{1-x}Zn_xTe$ film. The

data shows that higher anneal temperature does not help mitigate Zn depletion when using $CdCl_2$ vapor treatments. However, refinement of the $CdCl_2$ partial pressure and delivery and of treatment time may lead to retention of more Zn in the lattice during this essential treatment step.

The effect of vapor $CdCl_2$ treatment on un-annealed vapor transport deposited $Cd_{1-x}Zn_xTe$/CdS film structures was assessed by XRD analysis of the (111) $Cd_{1-x}Zn_xTe$ peak shape at three alloy compositions: x = 0, x = 0.3 and x = 0.8. The XRD peak profiles before and after annealing in 1 mTorr $CdCl_2$ vapor at 480°C for 2 minutes are shown in Figures 13, 14, and 15.

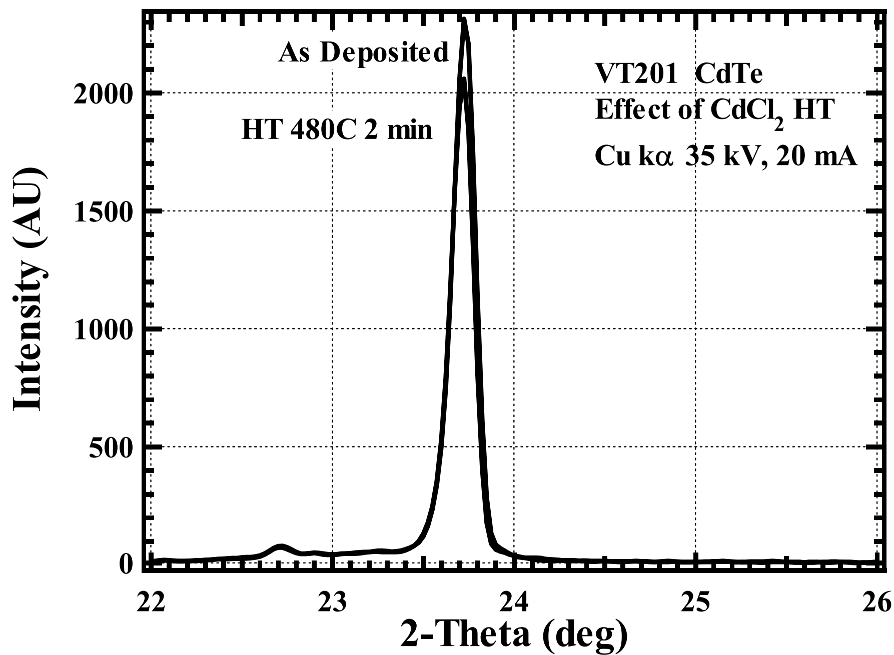

Figure 13. XRD peak profiles of CdTe (111) before and after short $CdCl_2$ vapor treatment.

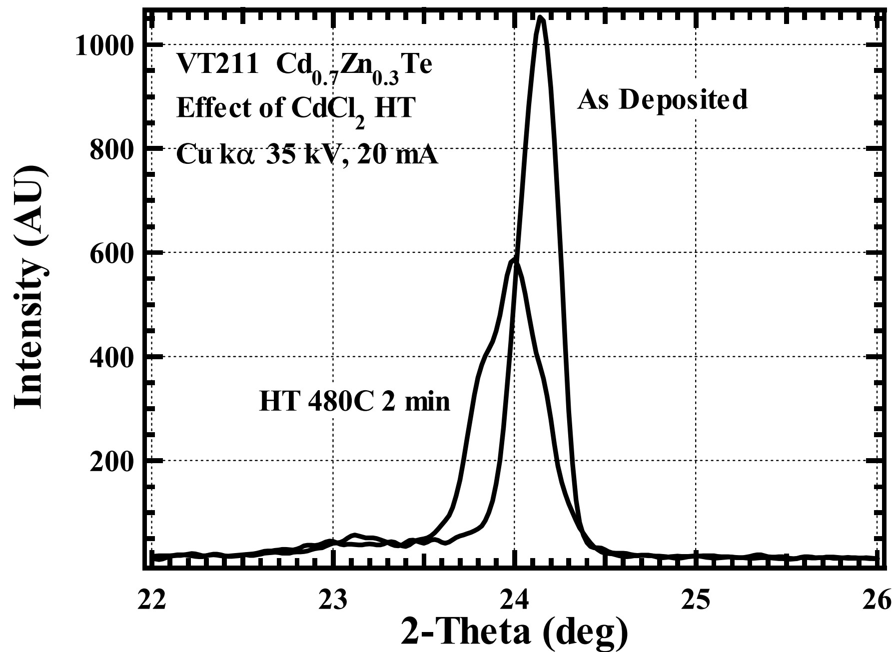

Figure 14. XRD peak profiles of $Cd_{0.7}Zn_{0.3}Te$ (111) before and after short $CdCl_2$ vapor treatment.

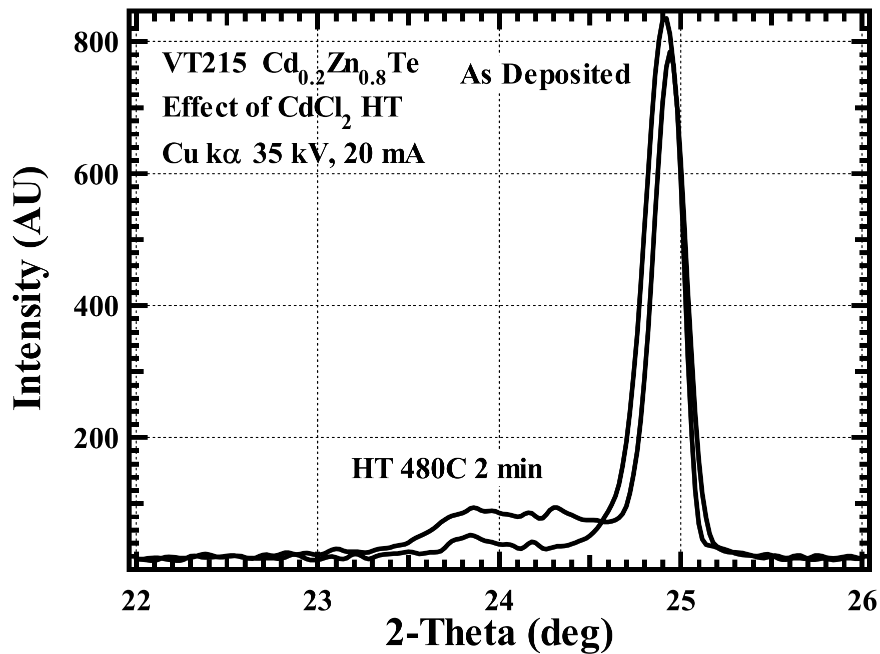

Figure 15. XRD peak profiles of $Cd_{0.2}Zn_{0.8}Te$ (111) before and after short $CdCl_2$ vapor treatment.

In Figure 13, for a CdTe/CdS structure, no significant change is measured in the diffraction peak intensity or distribution. In Figures 14 and 15, with alloy absorber films, however, a shift of the primary peak towards lower diffraction angle (higher d-spacing)

and development of a shoulder on the low-angle side both indicate zinc loss by a diffusion-controlled process, with development of nearly pure CdTe at the surfaces and gradual reduction of zinc content in the grain interiors. Comparing these results to those obtained during previous phases of this research, in which samples were treated in $CdCl_2$ vapor for up to 30 minutes, demonstrates the additional control that has been achieved with respect to bulk $Cd_{1-x}Zn_xTe$ grain composition by use of vapor treatments with reduced concentration of $CdCl_2$ and O_2 gas phase constituents. Recall that the conversion of ZnTe to CdTe in the presence of $CdCl_2$ vapor or solid is thermodynamically favored, with ΔH_f^o = -18.8 kcal/mol at 400°C. Thus, controlling ambient composition gives kinetic control, allowing electrical activation of the semiconductor structure with minimal Zn loss in the bulk absorber layer, and retention of the desired band gap.

3.4 Device Fabrication and Analysis

During the research period, cell fabrication with baseline CdS/Ga_2O_3/TEC15 substrates was complicated by two issues which were eventually ameliorated, specifically shunting in CdTe and $Cd_{1-x}Zn_xTe$ cells due to contamination in the HR buffer layer used on the window side of the device, and high lab humidity which caused rapid conversion of the back surface of $Cd_{1-x}Zn_xTe$ films to ZnO. Despite the batch processing issues, VT cells with $Cd_{1-x}Zn_xTe$ band gap of ~1.6 eV having high efficiency were fabricated. $Cd_{1-x}Zn_xTe$/CdS solar cells with x < 0.2 fabricated with $CdCl_2$ vapor treatment exhibit comparable performance to those treated in $ZnCl_2$ but are easier to process due to simpler handling required for $CdCl_2$ compared to $ZnCl_2$. As described in Section 3.4 above, control of the final absorber band gap is not as precise due to two thermodynamically favored processes: 1) conversion of the Zn component of the alloy to volatile $ZnCl_2$, resulting in less Zn in the final device absorber and 2) reaction of ZnTe with CdS to form ZnS and CdTe in the interface region.

Table VII shows performance data obtained for cells with different starting composition and band gap. After cell processing, the absorber band edge was shifted by ~40 nm compared to CdTe cells, indicating a final composition of x~0.15 in the junction region. In the table, the column labeled "QE @ 400 nm" contains the spectral response at 400 nm which is indicative of the final CdS thickness in CdTe/CdS cells. In our prior reports, we have documented the conversion of CdS to ZnS during the halide treatment, which is a strongly favored chemical reaction, verified for $Cd_{1-x}Zn_xTe$/CdS and ZnTe/CdS couples. Both cells in the table exhibited enhanced blue response compared to CdTe/CdS cells, due to partial conversion of the CdS layer to ZnS. Note that the highest V_{OC} was obtained for the cell with the lower response at 400 nm, corresponding to less conversion of the CdS and yielding a lower J_{SC}. In optimizing this process for efficiency, the tradeoff between the V_{OC} and J_{SC} will need to be addressed.

Samples from run VT233 yielded the highest performance, as shown in Table VII. All the films from sample 246, having x = 0.8, peeled off during processing, due to penetration of the HCl rinse to the window layer via pinholes arising from HR layer contamination. For most of the films subjected to $CdCl_2$ treatment, GIXRD analysis of the exposed window layer shows that as with previous cells having absorber layers over

this compositional range, the CdS layer completely converted to ZnS, with a resulting high short wavelength QE. As in the previous phase of research, V_{OC} values in the range 800-830 mV were achieved. We speculate that the inability to achieve higher Voc with wider bulk band gap, up to 1.6 eV, is due to the exchange reaction at the interface, converting $Cd_{1-x}Zn_xTe$ and CdS into CdTe and ZnS, with CdTe-like recombination in the absorber side of the junction. It was therefore decided to pursue alternative heteropartner materials with less chemical reactivity.

Table VII. JV and QE results for $Cd_{1-x}Zn_xTe$/CdS cells treated in $CdCl_2$ vapor.

Sample	x in alloy	V_{OC} (mV)	J_{SC} (mA/cm^2)	FF (%)	Eff (%)	QE @ 400 nm	QE edge (eV)
VT182.6a	0.20	835	20.0	66	11.0	50	1.57
VT233.5	0.13	832	26.0	65	14.0	78	1.58
VT182.5	0.20	811	23.0	66	12.3	58	1.58
VT245.3	0.16	416	18.1	42	3.2	78	1.63
VT250.4	0.26	381	21.8	45	3.8	77	1.63

The approach was evaluation of devices with pure ZnTe absorber layers and alternative window layers. Among II-VI compounds, the candidate materials for n-type buffer layers were the thermodynamically stable Zn compounds ZnO, ZnS and ZnSe. A close-space vapor transport (CSVT) system was configured for deposition of CdS, ZnS and ZnSe, while ZnO was deposited by rf sputtering. ZnS and ZnSe films were deposited at 550°C in Ar ambient using pyrolytic graphite susceptors with 6N purity source powders. ZnO was deposited at room temperature from an undoped ZnO target in Ar/O_2 ambient.

All devices were fabricated on ITO coated Corning 7059 borosilicate glass (ITO/BSG). The window layer films were deposited to thicknesses of ~100 nm and were characterized by optical transmission, GIXRD and AFM to ensure band gap, phase purity and in-plane continuity. ZnTe was also deposited by CSVT, at 575-600°C in argon ambient using a SiC coated graphite susceptor. The targeted ZnTe thickness for this experiment was 4 microns.

The completed structures were analyzed by XRD after ZnTe deposition to determine the extent of chemical interactions between the semiconductor layers. For ZnTe/ITO, ZnTe/ZnO, ZnTe/ZnO and ZnTe/ZnSe, no evidence was found for alloy formation during ZnTe deposition. However, CdS/ZnTe structures exhibited pronounced inter-reactivity, resulting in formation of a complex admixture of different alloys. Figures 16 and 17 show the XRD line profiles over the basal plane angular region for the II-VI materials, for ZnTe/CdS, ZnTe/ZnS and ZnTe/ZnSe. Linear and logarithmic intensity scales are used to highlight ZnTe (111) peak intensity profiles and interface phases, respectively. In Figure 16, peaks 1 and 2 correspond to a Cd-shifter ZnTe (111) peak for ZnTe/CdS and unshifted ZnTe (111) for ZnTe/ZnS and ZnTe/ZnSe. In Figure 17, peaks 1 and 2 are alloy-shifted ZnTe (111) and CdS (002), respectively. Peak 3 is ZnSe in the ZnTe/ZnSe structure. Peak 5 is ZnTe for ZnTe/ZnS and ZnTe/ZnSe and Cd-shifted ZnTe for ZnTe/CdS. The ZnS peak is not detected in the full film stack, due to low atomic scattering factor for and to attenuation by the overlying ZnTe.

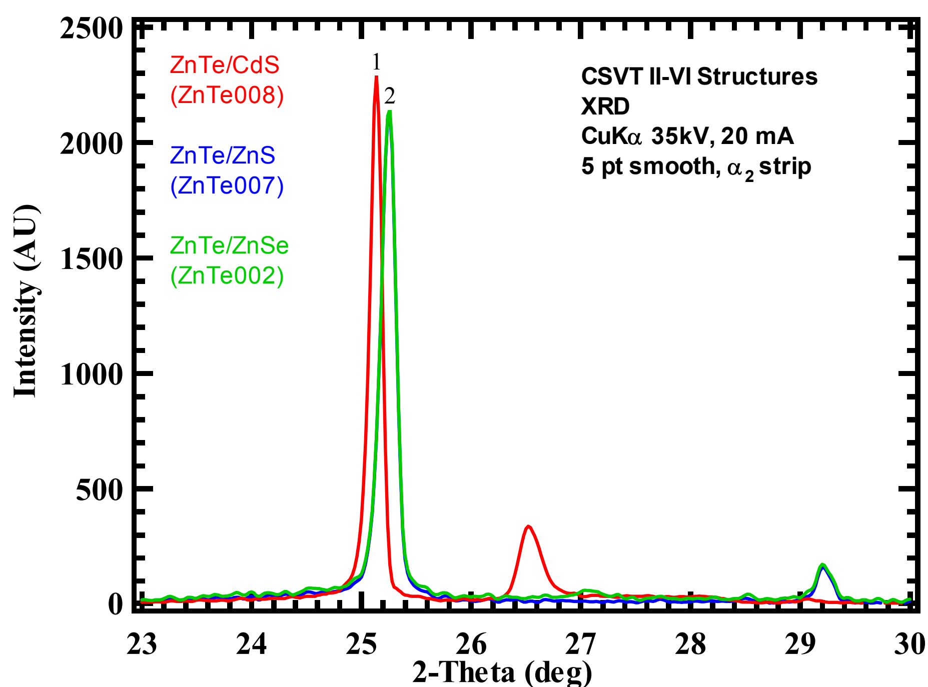

Figure 16. XRD peak profiles of as-deposited ZnTe/CdS, ZnTe/ZnS and ZnTe/ZnSe on a linear intensity scale.

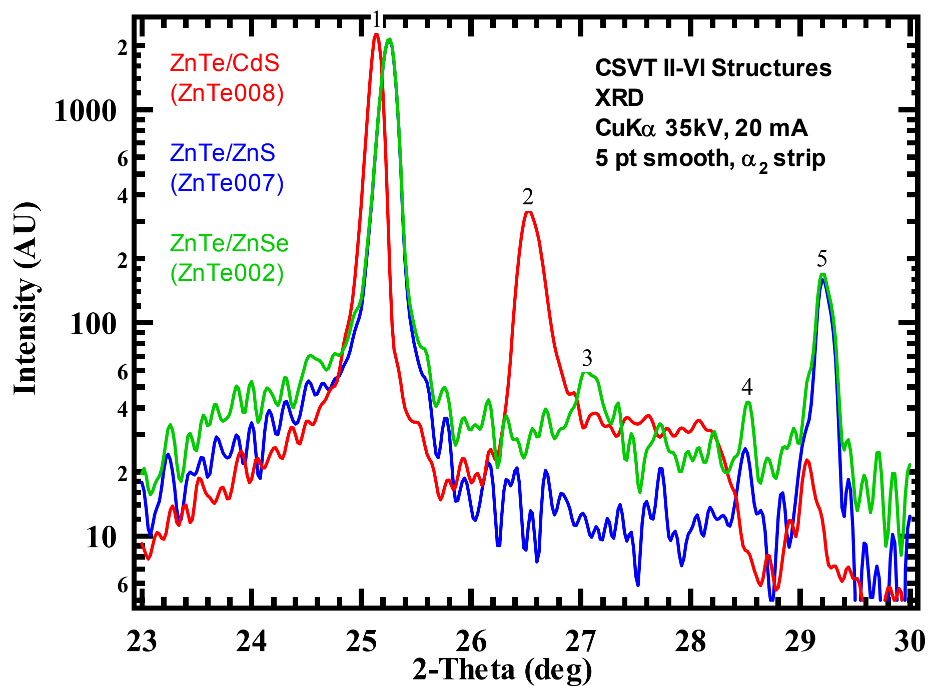

Figure 17. XRD peak profiles of as-deposited ZnTe/CdS, ZnTe/ZnS and ZnTe/ZnSe on a logarithmic intensity scale to highlight weak reflections.

Devices were completed by treatment in 1 mTorr $ZnCl_2$ vapor at 480°C for 2 minutes, followed by etching in HCl to remove surface ZnO, then etching in aniline solution for 1 minute to form a thin Te surface layer. Cells were made on each piece with and without the addition of copper. For cells with copper, a 2 nm Cu film was deposited by electron beam evaporation onto the Te surface. Graphite paste dot contacts were applied as robust contacts for current-voltage (JV) and quantum efficiency (QE) measurements. Cell results fell into two groups based on the use of Cu in the back contact: cells without Cu exhibited $J_{SC} << 1$ mA/cm^2 in all cases, and cells with Cu typically exhibited higher J_{SC}. V_{OC} was largely unaffected by the use of Cu. The cell structure and best cell JV results on devices made with Cu are listed in Table VIII. The JV and QE characteristics for ZnTe/ZnS and ZnTe/ZnSe are shown in Figures 18 and 19, respectively.

Table VIII. JV results for ZnTe cells with different buffer layers on ITO/BSG substrates. using Cu/C back contacts.

Sample	Buffer	Thk (nm)	Method	V_{OC} (mV)	J_{SC} (mA/cm^2)	FF (%)	Eff (%)
01	none	-	-	134	0.1	25	0
15	ZnO	100	Sputter	74	1.0	25	0
09	CdS	120	CSS	45	0.2	25	0
62	ZnS	100	CSS	446	5.4	26	0.6
17	ZnSe	120	CSS	552	6.9	27	1.0

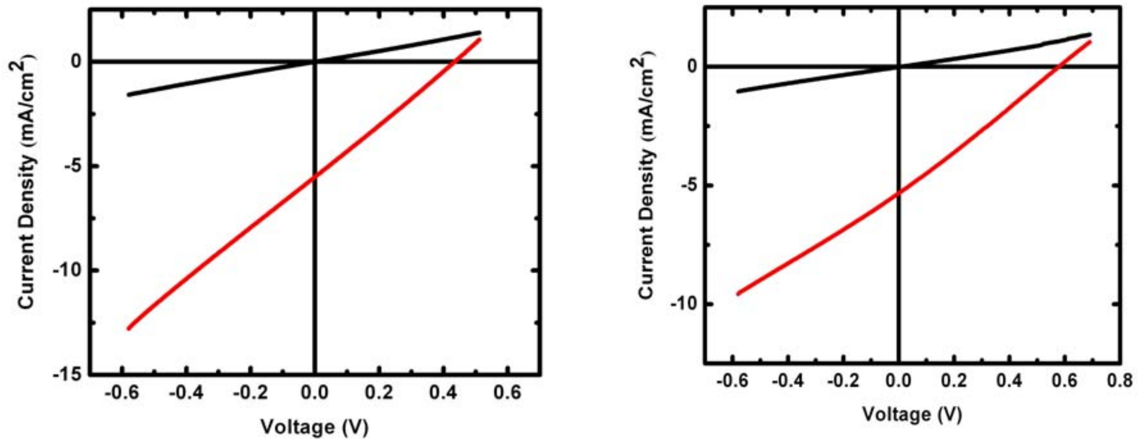

Figure 18. Dark and AM1.5 JV characteristics of ZnTe/ZnS (left) and ZnTe/ZnSe (right).

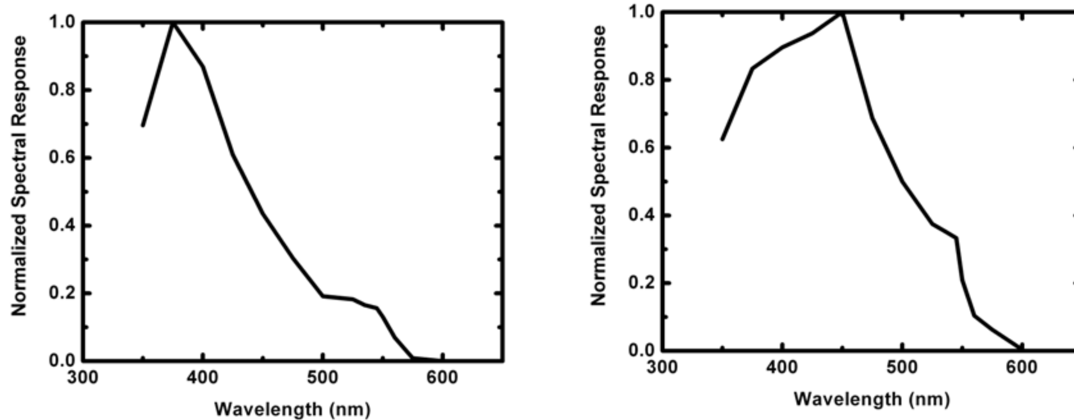

Figure 19. Normalized spectral response (dark, 0V)of ZnTe/ZnS (left) and ZnTe/ZnS (right).

Overall, the JV characteristics of the best ZnTe cells, with ZnS and ZnSe heteropartners exhibited dark shunting coupled with high series resistance. These deleterious circuit elements were apparent in the light JV characteristics and account for the low fill factors obtained with the light JV measurements. Comparable current densities were obtained with ZnS and ZnSe but the ZnSe exhibited consistently higher open circuit voltages. The expected light generated current for a ZnTe cell with QE = 1 from 350 to 540 nm is ~9.3 mA/cm^2 so the cells fabricated in this work have over half of the expected current density. The spectral response characteristics show a rise from 350 nm, and a peak near the band gap of the respective heteropartner layers, viz, ZnS at 370 nm (λ at E_g = 340 nm) and ZnSe at 450 nm (λ at E_g = 464 nm). These spectral response characteristics suggest current generation and collection in the ZnS and the ZnSe, unlike CdTe/CdS devices in which the CdS does not contribute significantly to current generation in the device. The present results with ZnTe/ZnS and ZnTe/ZnSe junctions exceed those we have obtained with ZnTe/CdS junctions and their attendant chemical instability. This strongly suggests that a viable path for development of $Cd_{1-x}Zn_xTe$ cells with band gaps in the 1.6 to 1.8 eV range may be facilitated by use of the ZnSe heteropartner and that the optimization process will need to rely on controlling the ZnSe film properties.

4.0 Collaborations

4.1 University of Oregon

$CuGaSe_2$ devices were prepared for analysis at U. of Oregon and comparison to previous measurements on devices with $Cu(InGa)Se_2$ with varying relative Ga concentration and $Cu(InGa)(SeS)_2$. The $CuGaSe_2$ was deposited using single layer evaporation with substrate temperature ≈ 550°C. Formation of $CuGaSe_2$ with uniform lateral morphology required the layers to be deposited with very high Se flux, [Se]/[Cu] >> 10. The devices along with the absorber layer composition expressed as [Cu]/[Ga] are listed in Table IX. These films are relatively low in Cu. Films with higher Cu content gave poorer device performance.

Table IX. $CuGaSe_2$ devices fabricated for analysis at U. of Oregon.

Sample #	[Cu]/[Ga]	η (%)	V_{OC} (V)	J_{SC} (mA/cm^2)	FF (%)
33999.22	0.56	5.7	0.811	10.4	67.2
34000.21	0.78	5.6	0.864	10.4	62.4

Another set of $Cu(InGa)Se_2$ films were grown to characterize the effect of Na on the device properties and the devices were sent to U. of Oregon for analysis. These samples were deposited at 550°C in a single standard $Cu(InGa)Se_2$ run # 34017. This run had thickness 2.0 μm with composition measured by EDS of 22.9% Cu, 19.0% In, 6.6% Ga, and 51.6% Se. One sample was deposited on a soda lime (SL) glass substrate with an SiO_2 barrier layer, intended to limit Na diffusion from the glass, followed by a sputtered Mo contact. This substrate was provided by Shell Solar. The control sample was deposited on IEC's baseline Mo-coated soda lime glass substrate. The performance of these devices is compared in Table X and Figure 20. The substrate with the SiO_2 barrier lead to devices with lower V_{OC} and evidence of a blocking barrier in forward bias. Similar sets of samples may be fabricated with other $Cu(InGa)(SeS)_2$ alloys in the future.

Table X. J-V parameters of $Cu(InGa)Se_2$ devices with and without a Na diffusion barrier, fabricated for analysis at U. of Oregon.

Sample #	[Cu]/[Ga]	η (%)	V_{OC} (V)	J_{SC} (mA/cm^2)	FF (%)
34017.12	SL glass	15.5	0.620	33.6	74.6
34017.32	barrier-coated SL	10.7	0.492	33.0	66.0

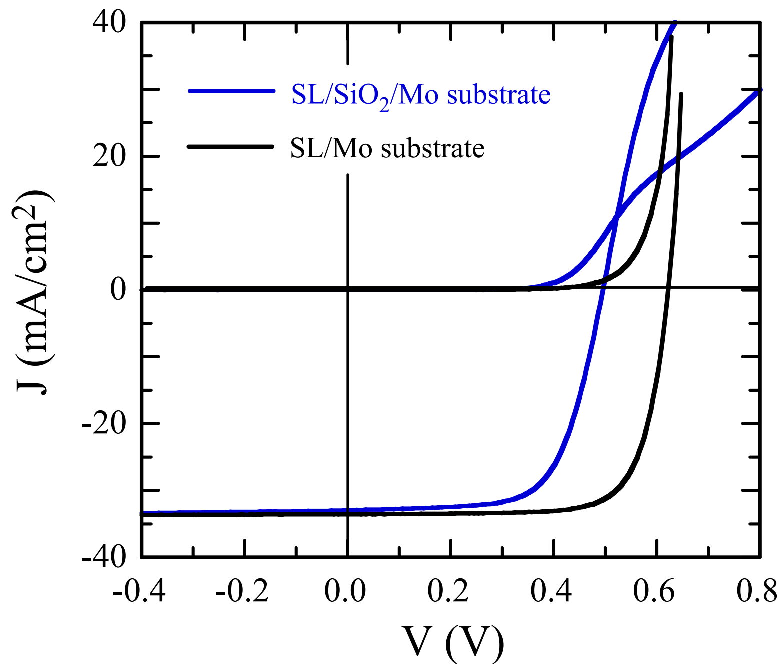

Figure 20. J-V curves of $Cu(InGa)Se_2$ devices with and without a Na diffusion barrier.

Two papers resulting from this collaboration were presented at the 4th World Conference on Photovoltaic Energy Conversion:

"Role of Bulk Defect States in Limiting CIGS Device Properties," JinWoo Lee, Jennifer T. Heath. J. David Cohen and William N. Shafarman, Proc. 32nd IEEE PVSC and WCPEC-4, 360 (2006).

"Electronic Properties of Wide Bandgap Pentenary Chalcopyrite Alloys and their Photovoltaic Devices," Adam Halverson, Shiro Nishiwaki, William Shafarman and J. David Cohen, Proc. 32nd IEEE PVSC and WCPEC-4, 364 (2006).

References

1. A. Stavrides, C. Yapp, W. Shafarman, R. Aparicio, R. Opila, and R. Birkmire, Proc. 31st IEEE PVSC, 247 (2005).
2. B. E. McCandless, W. A. Buchanan, G. M. Hanket, Proc. 32nd IEEE PVSC and WCPEC-4, 483 (2006).
3. R. Klenk, T. Walter, D. Schmid, and H. W. Schock, Jpn. J. Appl. Phys. Suppl. **32**, 57 (1993).
4. T. Walter, D. Braunger, H. Dittrich, Ch. Köble, R. Herberholz, and H. W. Schock, Sol. Energy Mater. Sol. Cells **40-41**, 355 (1996).
5. W.N. Shafarman and L. Stolt, Chapter 13 in Handbook of Photovoltaic Science and Engineering, ed. by A. Luque and S. Hegedus, John Wiley & Sons, Ltd., 567 (2003).
6. W.N. Shafarman and J. Zhu, Thin Solid Films **361-362**, 473 (2000).
7. S. Nishiwaki, and W. N. Shafarman, Proc. WCPEC-4, 461 (2006).
8. M. Gossla and W. N. Shafarman, Thin Solid Films **480-481**, 33 (2005).
9. P. D. Paulson, R. W. Birkmire, and W. N. Shafarman, J. Appl. Phys. **94**, 879 (2003).
10. B. W. Liang and C. W. Tu, J. Appl. Phys. **74**, 255 (1993).
11. B. Meyer, Chem. Rev. **76**, 367 (1976).
12. L. S. Brooks, J. Am. Chem. Soc. **74**, 227 (1952).
13. T. I. Koneshova, Izv. Akas. Nauk. SSSR, Neorg. Mater. **18**, 1783 (1982).
14. J. C. Mikkelsen, Jr. and J. J. M. Binsma, J. Electronic Mater. **20**, 541 (1981).
15. J. J. M. Binsma, L. J. Giling, and J. Bloem, J. Cryst. Growth **50**, 429 (1980).
16. M. Kokta, J. R. Carruthers, M. Grasso, H. M. Kasper, and B. Tell, J. Electronic Mater. **5**, 69 (1976).
17. I. V. Bologa, Thermochimica Acta **93**, 685 (1985).
18. D. Cahen and R. Noufi, J. Phys. Chem. Solids **52**, 947 (1991).
19. S. Kosaraju, I. Repins, and C. A. Wolden, Mat. Res. Soc. Symp. Proc.**763**, B8.19.1, (2003).
20. H. Migge and J. Grzanna, J. Mater. Res. **9**, 125 (1994).
21. H. Rau and A. Rabenau, J. Solid State Chem. **1**, 113 (1994).
22. H. Rau, J. Phys. Chem. Solids **35**, 1415 (2974).
23. B. Brunette, V. Piacente, and P. Scardala, J. Alloys Comp. **206**, 113 (1994).
24. A. Yu Egorov, A. R. Kovsh, V. M. Ustinov, A. E. Zhukov, P. S. Kopém, and C. W. Tu, J. Cryst. Growth **188**, 69 (1998).

REPORT DOCUMENTATION PAGE

Form Approved
OMB No. 0704-0188

The public reporting burden for this collection of information is estimated to average 1 hour per response, including the time for reviewing instructions, searching existing data sources, gathering and maintaining the data needed, and completing and reviewing the collection of information. Send comments regarding this burden estimate or any other aspect of this collection of information, including suggestions for reducing the burden, to Department of Defense, Executive Services and Communications Directorate (0704-0188). Respondents should be aware that notwithstanding any other provision of law, no person shall be subject to any penalty for failing to comply with a collection of information if it does not display a currently valid OMB control number.

PLEASE DO NOT RETURN YOUR FORM TO THE ABOVE ORGANIZATION.

1. REPORT DATE *(DD-MM-YYYY)*	**2. REPORT TYPE**	**3. DATES COVERED** *(From - To)*
August 2008	Subcontract Report	6 November 2003 - 5 January 2007

4. TITLE AND SUBTITLE
Development of a Wide Bandgap Cell for Thin Film Tandem Solar Cells: Final Technical Progress Report, 6 November 2003 - 5 January 2007

5a. CONTRACT NUMBER
DE-AC36-99-GO10337

5b. GRANT NUMBER

5c. PROGRAM ELEMENT NUMBER

6. AUTHOR(S)
W. Shafarman and B. McCandless

5d. PROJECT NUMBER
NREL/SR-520-42388

5e. TASK NUMBER
PVA72401

5f. WORK UNIT NUMBER

7. PERFORMING ORGANIZATION NAME(S) AND ADDRESS(ES)
Institute of Energy Conversion
University of Delaware
Newark, Delaware 19716

8. PERFORMING ORGANIZATION REPORT NUMBER
XAT-4-33624-01

9. SPONSORING/MONITORING AGENCY NAME(S) AND ADDRESS(ES)
National Renewable Energy Laboratory
1617 Cole Blvd.
Golden, CO 80401-3393

10. SPONSOR/MONITOR'S ACRONYM(S)
NREL

11. SPONSORING/MONITORING AGENCY REPORT NUMBER
NREL/SR-520-42388

12. DISTRIBUTION AVAILABILITY STATEMENT
National Technical Information Service
U.S. Department of Commerce
5285 Port Royal Road
Springfield, VA 22161

13. SUPPLEMENTARY NOTES
NREL Technical Monitor: Fannie Posey Eddy

14. ABSTRACT *(Maximum 200 Words)*
The objective of this research program was to develop approaches for a transparent wide-bandgap cell to be used in a thin-film tandem polycrystalline solar cell that can ultimately attain 25% efficiency. Specific goals included the research and development of Cu(InGa)(SeS)2 and Cd1-xZnxTe alloys with a bandgap from 1.5 to 1.8 eV, demonstrating the potential of a 15% cell efficiency with a transparent contact, and supporting the High Performance PV Program. This Final Report presents results that emphasize the 3rd phase of the program.

15. SUBJECT TERMS
PV; wide bandgap; solar cell; thin film; tandem polycrystalline; transparent contact; high efficiency; deposition; vapor transport; device fabrication;

16. SECURITY CLASSIFICATION OF:			**17. LIMITATION OF ABSTRACT**	**18. NUMBER OF PAGES**	**19a. NAME OF RESPONSIBLE PERSON**
a. REPORT	**b. ABSTRACT**	**c. THIS PAGE**			
Unclassified	Unclassified	Unclassified	UL		**19b. TELEPHONE NUMBER** *(Include area code)*

Standard Form 298 (Rev. 8/98)
Prescribed by ANSI Std. Z39.18